Catalysis Today 433 (2024) 114655

Contents lists available at ScienceDirect

Catalysis Today

journal homepage: www.elsevier.com/locate/cattod

Copper, potassium promoted iron on metallosilicate and aluminum oxide supports synthesized via a non-hydrolytic sol-gel for Fischer-Tropsch

Tugce N. Eran [a,*], Federico Galli [b], Jean Guyot [a], Josianne Lefebvre [a], Arian Grainca [c], Gregory Patience [a], Carlo Pirola [c]

[a] Polytechnique Montréal, CP 6079, Succ CV, Montréal, Québec H3C 3A7, Canada
[b] Université de Sherbrooke, 2500 Boul. de l'Université, Sherbrooke, Québec J1K 2R1, Canada
[c] Università degli Studi di Milano, Chimica, via Golgi 19, Milano 20133, Italy

ARTICLE INFO

Keywords:
Fischer-Tropsch
Fe catalyst
Metallosilicates
Promoters
Non–hydrolytic sol–gel

ABSTRACT

We developed a promoted iron based catalyst that converts 20% more CO to diesel than the unpromoted counterparts. The synthesis involves a non-hydrolytic sol-gel method (NHSG) and 0.04 g g^{-1} copper and 0.02 g g^{-1} potassium as promoters. The iron catalyst supports included cerium and zirconium metallosilicates and Catalox and Dispal commercial aluminum oxides from Sasol. At 325 °C and 20 bar, CO conversion over the Fe/Ce/SiO_2-K,Cu, exceeded 85% while at the same conditions it was only 68% over the unpromoted catalyst. Fe/Zr/SiO_2-K,Cu converted less CO than the cerium-silicate (75%) but the unpromoted zirconium-silicate only converted 43% of the CO. The conversion and selectivity of the Catalox was about the same as the cerium-silicate, while the Dispal performance was equivalent to the zirconium-silicate. This study also highlights the importance of support and promoters in FTS, demonstrates the potential of the NHSG method to synthesize promoted iron catalysts with various supports and lays the foundation for developing efficient and stable catalysts for converting syngas to hydrocarbons.

1. Introduction

As society adopts alternative energy sources to meet industrial and residential needs, several hard to convert sectors like shipping, jet fuel, and long haul trucking will continue to rely on diesel fuel. Biomass, wasted natural gas (flared, bio-gas, landfill gas), and anthropogenic atmospheric CO_2 are green alternatives to petroleum as a bridge-solution for these sectors in which the carbon is converted to CO and reacts with H_2 over Co or Fe catalyst—Fischer-Tropsch synthesis (FTS). Fischer Tropsch synthesis (FTS) was developed one-hundred years ago and is now a corner-stone of gas-to-liquid processes with feedstocks like coal, natural gas, biomass, and even anthropogenic CO_2. In the latter case, CO_2 is converted to CO via the reverse water gas shift reaction. FTS is a more sustainable and environmentally friendly energy vector. The main objectives of FTS studies are principally to identify the optimal combination of catalyst structure and operating conditions to maximize C_{5+} hydrocarbon selectivity and CO conversion [1–4,5]. Here we developed and compared various supports for promoted iron catalysts. We also examined the impact of a non-hydrolytic sol-gel method with various promoters. Comparing the promoted and un-promoted iron based catalyst activity on Fischer Tropsch synthesis has been extensively studied and documented [6–9,10,11]. Group 1A alkali metals, especially K, are common and efficient promoters for iron. Potassium increases the average molecular weight of the hydrocarbon products, as reported, for example, in a study with a fixed bed operating at 14.8 bar, 235°C < T < 265°C at a syngas ratio H_2:CO=1 [12] Even though copper has a similar effect on the hydrocarbon selectivity, it slightly increases secondary reactions towards alcohols and olefins. Adding both promoters improved FTS and maintains stability for 200 h compared to a single promoted catalyst [13]. Potassium donates electrons to iron, which facilitates CO chemisorption. When H_2 covers the surface, it donates electrons to iron as well, but having an alkali metal (electron donating K) lowers the electron affinity of H_2, which weakens the Fe-H bond [14]. This phenomenon decreases the H_2 chemisorption while promoting CO chemisorption [14]. Metal-carbon bond strength increases while carbon-oxygen bond strength decreases, which makes it easier for hydrogen to remove oxygen and increase the FTS reaction rate. Potassium promotion prevents iron reduction, which means that catalyst

* Corresponding author.
E-mail address: nazmiye-tugce.eran@polymtl.ca (T.N. Eran).

https://doi.org/10.1016/j.cattod.2024.114655
Received 5 September 2023; Received in revised form 6 March 2024; Accepted 17 March 2024
Available online 20 March 2024

needs more time to reach steady-state. Copper facilitates iron reduction from Fe_2O_3 to Fe_3O_4, which accelerates the time to reach steady-state and further boosts the heavy hydrocarbon fraction. Cu-K promotes the formation of oxygen deficient iron oxide species and eventually reduces the Fe oxide crystallite size while forming carbides during the activation [15]. Even though Cu increases the tendency to form CH_4, K mitigates this trend.

Promoter loading also changes the structure and activity of the catalyst and FTS rate. For a Fe/Cu/SiO_2 catalyst, the Fe-O-Si interaction weakens as the K loading increases up to 7% [16]. The relationship between catalyst performance and loading also depends on catalyst structure, active phase loading, crystallinity, type of support, feed composition, temperature and pressure. In our previous study, we developed a non-hydrolytic sol-gel (NHSG) method to prepare metallosilicate supported iron catalysts [17]. The advantages of sol-gel chemistry include high purity, ability to control the structure, texture, and homogeneity [18,19] when applied for the synthesis of FT catalysts. Sol-gel chemistry depends on multiple factors such as temperature, solvent, aging and drying conditions, water content, and the nature of the precursors. The main problem with conventional sol-gel methods is the variation of reaction rates for different mixed oxide precursors. Hydrolysis and condensation rate of each precursor impacts the homogeneity directly. Another issue is the presence of water, with the accompanying capillary forces, which collapse the pore network, so an extra step is necessary such as supercritical drying, solvent exchange and/or applying a templating agent [20–23]. In conventional NHSG techniques, metal chloride precursors react with primary and secondary alcohols to form metal alkoxide. The alkoxides continue to react with metal chlorides. Another recipe applies tertiary and benzylic alcohols but the catalyst structure with this route is hard to control. The disadvantage of using metal alkoxide precursors is the high reaction temperature (200 °C to (numerical range) 250 °C) [24,25]. In our study, we chose to use a simple and commonly available material, iron nitrate, as a precursor to synthesize the catalysts. Based on the high CO conversion and HC selectivity observed in our previous study, we believe that further investigation into the reaction route and kinetics with nitrates in non-hydrolytic sol-gel method is an interesting topic, seldom investigated in FTS devoted literature. Four different catalysts were prepared by NHSG method and studied in this paper. Two samples were synthesized by preparing metallosilicate supports based on Ce or Zr and then by adding iron and promoters (K,Cu). Another two samples were synthesized with the same methodology over Catalox and Dispal commercial supports from Sasol. The goal of the preparation of these last two samples is to compare homemade metallosilicate supported catalysts with industrial supports. This exercise provides a universal reference, very rare in the FT scientific literature, so that other might benchmark their catalyst. For the reason of industrial secrecy, the characterization data on the catalysts prepared starting from commercial supports and some aspects of synthesis methodology will be limited in this article.

In summary, the four catalysts investigated in the present work are: (1) Fe/Ce/SiO_2-K,Cu (2) Fe/Zr/SiO_2-K,Cu (3)Fe/Catalox-K,Cu (4) Fe/Dispal-K,Cu all prepared by NHSG methods. The results for the samples (1) and (2) can be directly compared with the data published in [17] for the same catalysts in the absence of K and Cu promoters.

The catalysts were fully characterized and tested in FTS in terms of CO conversion and product selectivity (CO_2, CH_4, hydrocarbons with less than 7 carbon atoms, i.e. C_{7-} and hydrocarbons with 7 or more carbon atoms, i.e. C_{7+}) using syngas (H_2/CO mixture) as feeds. We also examined the impact of NHSG method on aluminum oxide support and compared the characteristic aspects and catalytic activity.

2. Experimental

2.1. Materials

Zirconium(IV) ethoxide (97%, solid), ammonium cerium(IV) nitrate ($\geq$ 99.99%, trace metal basis), iron nitrate nonahydrate (98%, bioreagent) tetraethyl orthosilicate (TEOS, $\geq$ 99.0%), tetraethylammonium hydroxide solution (TEAOH, 35% in aqueous solution), potassium nitrate (ReagentPlus $\geq$ 99.0%), and copper(II) acetate mono hydrate (ACS reagent, $\geq$ 98%) were procured from Aldrich and used as received. The structure directing agent, triethanolamine (TEA,$\geq$ 99%), pluronic P123 (block polymer-poly(ethylene glycol)- block-poly(propylene glycol)-block- poly(ethylene glycol)) were procured from Aldrich. Reagent alcohol (90.2% ethanol, balance methanol and iso-propanol) was purchased from LabChem, UN1987). Dispal ®T 25N4–80 (boehmite) Alumina and Catalox ®SCCa 5/110 Alumina oxides were both acquired from Sasol Chemicals (USA) LLC.

2.2. Support synthesis

We synthesized the supports based on previous literature [17]. TEOS was mixed with metal precursors (1:10 molar M_xO_y: SiO_2) and stirred for 30 min. Then TEA (mesopore directing agent) was added to this solution and mixed another 30 min. Later the water was added drop wise and the solution was stirred another 60 min. Finally, TEAOH was added to the mixture and the solution was left to age for 24 h. The molar ratio of the resulting gel was 1 SiO_2:0.1 M_xO_y: 0.3 TEA:0.1 TEAOH:11 H_2O, where M is Ce or Zr based on the choice of the support. We dried the resulting gel at 100 ˚C for 24 h and calcined it for 10 h at 700 ˚C.

2.3. Catalyst preparation

We used the same non-hydrolytic sol-gel synthesis method as a previous study [17]. The ethanol (25 mL) and block copolymer P123 (1.8 g) were mixed until the template is homogeneous (40 min to (numerical range) 45 min). Then supports (Catalox, Dispal or metallosilicate, 3 g) and 0.10 g g^{-1} iron nitrate nonahydrate were added to this solution slowly. To improve the homogeneity, we mixed the solution for 30 min at 40 ˚C then we added the K (potassium nitrate) and Cu (copper(II) acetate mono hydrate) precursors. We used 0.020 g g^{-1} K and 0.038 g g^{-1} Cu as a promoter. After adding the promoters, we continued mixing for 20 min at 40 ˚C. Later, the final solution was placed into a petri dish and left to gel in the oven at 40 ˚C with relative humidity of 50%. The gel aged for 5 days and we collected the catalyst which at this stage was still partially humid due to the moisture retained in the gelation process. The same procedure of drying and calcining of supports was followed for all 4 catalysts. The collected particles dried at 100 ˚C for 24 h and calcined at 700 ˚C for 10 h with a heating rate of 1 ˚C/min in air in air.

2.4. Characterization

The following instruments were applied to characterize the catalyst samples: LEO 1525 ZEISS (Jena, Germany) SEM evaluated the morphology of the samples [17]. Field emission scanning electron microscopy was applied at an accelerating voltage of 15 kV for 2 min. A Brunker Quantax EDX instrument coupled to the SEM mapped the surface elemental distribution.

The SEM was a JEOL JSM-7600 F with a field emission gun (FEG) and a maximum resolution of 1.0 nm at 15 kV. Images can be acquired in both secondary electrons (topographic contrast) and backscattered electrons (chemical contrast). It is equipped with an Oxford X-Max N EDS detector which has an active area of 80 mm^2 and a spectral resolution of 123 eV at 5.9 keV.

Micromeritics (Tristar II 3020) determined the Brunauer-Emmett-Teller (BET) specific surface area of the samples and measured the adsorption/desorption isotherms from N_2 at − 196˚C. The Barrett-Joyner-Halenda (BJH) method was applied to determine the porosity distribution. To remove the contaminants and adsorbed water, the samples were pre-treated at 150 ˚C under He flow for 4 h.

A Philips PW1710 diffractometer generated the X-Ray powder

diffraction (XRD) patterns. The CuK_α radiation was performed with the operating conditions set at 40 kV and 20 mA. The step scan rate was maintained at 1 ˚C/min and a counting time 1 s per step was applied. The 2α range spanned from 0˚ to (numerical range) 90˚.

D8 Advance Plus Bruker X-Ray Diffration analyzed the cyrstallinity of the materials. The X-ray generator was set to 40 kV and 40 mA.

X-ray photoelectron spectroscopy (XPS) analysis was performed using an Escalab 250Xi (Thermo Fisher Scientific) with a monochromated Al Kα source at a power of 218.8 W (14.7 kV, 14.9 mA), a 180˚, double-focusing,bipolar hemispherical analyzer, and standard charge compensation using low energy electrons and Ar^+. The pressure in the analysis chamber during the measurement was kept below $2x10^{-7}$ mbar. Survey spectra were acquired at a pass energy of 150 eV and a step size of 1.0 eV. High resolution spectra were acquired at 20 eV pass energy and a step size 0.1 eV. This yields a FWHM for the ester peak in polyethylene terephthalate (PET) of 0.81 eV. Based on typical values for electron attenuation length this yields an XPS analysis depth of 5 nm to (numerical range) 10 nm for a flat surface. Data processing was performed using Avantage v6.5.0 (Thermo Fisher Scientific). All elements present on the surface (except H and He which are not detected by XPS) were identified from survey spectra. Their atomic concentrations were calculated using integral peak intensities and the sensitivity factors supplied by the manufacturer. Binding energies were referenced to the C1s peak at 285.0 eV for aliphatic hydrocarbons.

2.5. FT bench scale reactor

The catalysts were tested using the same apparatus as in a previous work [17]. CO, H_2, N_2(as internal analytical standard) were regulated by Brooks flowmeters and fed to the fixed bed reactor. The catalysts were placed, without dilution, in a 6 mm internal diameter packed bed and a GHSV = 2805 h^{-1}. The catalyst bed was held in place with quartz wool. A K-type thermocouple measured the temperature inside the catalytic bed. To activate the catalyst, we introduced a mixture of H_2 and CO (in a 2:1 molar ratio) with a flow rate of 53 NmL/min, while maintaining the temperature at 350 ˚C and pressure at 20 bar for a duration of 4 h. We assumed time zero as we reach the required temperature and pressure. After the reactor, a 0.13 L cold trap maintained at 5 ˚C and 20 bar, collected the condensed reaction products, i.e. water and heavy hydrocarbons liquid. We only collected liquid products from C_5 to C_{20} in a cold trap while the effluent was monitored by GC [26]. A back pressure regulator maintained the reactor at 20 bar during FT test, after the activation step. An Agilent 3000A micro gas chromatograph analyzed the permanent gases ($N_2$and non converted H_2 and CO) and non-condensable hydrocarbons so we determined the CO conversion (X_{CO}) based on N_2 and CO peak areas (A_{N_2} and A_{CO}) their relative response factor (k), and inlet (set) flowrate of CO and N_2 (F_{in,N_2}, and $F_{in,CO}$) (Eq. (1)). The selectivity of desired product(s) ($S_{product}$) was determined as stated in the Eq (2) [17]. QPLOT columns and molsieves are installed in the instrument. He was the carrier gas and GC oven was maintained the column temperature at 50 ˚C. The micro GC sampled the effluent every 2 h. To ensure the accuracy and reliability of the experimental data, detailed carbon mass balance calculations were conducted for the FTS experiments. These calculations involved quantifying the input moles of carbon from CO and the output moles from all produced hydrocarbons and unreacted CO. The analysis indicated that the carbon balance error for each of the four catalysts tested remained below 5%. This result confirms the fidelity of the experimental data, accurately reflecting the catalysts' performance in the conditions tested. We determined the alpha (α) values, representing the probability of chain growth during Fischer-Tropsch synthesis, using the Anderson-Schulz-Flory distribution model(Eq (3))(Eq (4)) where W_n is the mole fraction of a hydrocarbon with chain length n, n is total carbon atom number, α is the probability of chain growth ($\alpha < 1$) and (1-α) is the probability of chain terminations [27]. This model is pivotal for predicting the distribution of hydrocarbon chain lengths produced in FTS, offering insights into the efficiency and selectivity of the catalysts under study.

$$X_{CO} = \frac{F_{in,\,CO} - F_{in,\,N_2} \cdot k \cdot \frac{A_{CO}}{A_{N_2}}}{F_{in,CO}} * 100 \quad (1)$$

$$S_{product} = \frac{\text{moles of desired product(s)}}{\text{moles of } CO_{in} - \text{moles of } CO_{out}} * 100 \quad (2)$$

$$\frac{W_n}{n} = (1-\alpha).\alpha^{(n-1)} \quad (3)$$

$$\ln(\alpha) = n\ln(\alpha) + \ln\left[\frac{(1-\alpha)^2}{\alpha}\right] \quad (4)$$

3. Results and Discussion

3.1. Characterization

SEM-EDS analysis identified Fe, Ce, Si, K and Cu in blue, cyan, magenta, green and yellow, respectively (Fig. 1) for the Fe/Ce/SiO_2-K, Cu catalyst. Based on the brightness of the images, Ce is the most well distributed on the surface. Fe and Si were distributed fairly well but some of the iron particles are embedded inside of the matrix. There were few islands of iron particles on the surface but they were mostly located below the cerium. Si particles were both located on the surface and in the core most likely. Si has a tendency to make weak connections with iron. So, it is possible that Fe is located around the Si [28,29]. K and Cu promoters on the other hand, were homogeneously distributed. However, since their mass loading is quite low, the images appear darker compared to the rest of the elements. The mixed image also showed that cerium was mostly distributed on the surface of the catalyst while silica appeared more as small islands on the surface. We detected iron species more clearly but it is clouded by the presence of other elements.

SEM images for Fe/Zr/SiO_2-K,Cu demonstrated Fe, Zr, Si, K and Cu in blue, yellow, magenta, orange and green respectively (Fig. 2). The iron particles were located predominantly on the zirconium silica supported catalyst surface and their distribution were more homogeneous compared to cerium silicate supported catalyst. Si was more heterogeneously distributed on the surface. K and Cu behaves similarly in both catalysts and distributed relatively homogeneously and located mostly below the surface of the catalyst. Also, SEM analysis is conducted on a limited number of spots, which may not accurately represent the entire structure of the catalyst.

Compared to the non-promoted catalysts [17], both metallosilicate supported catalysts are less porous and more rigid (Fig. 3). Non-promoted catalysts had a sponge like structure that facilitates the flow of reactants through the openings, mostly for Fe/Ce/SiO_2 rather than Fe/Zr/SiO_2 catalyst [17]. The extra metal deposition (promoter addition) on the catalyst surface fills the porous structure of the catalyst and narrows the pores (Fig. 3,b-1 and b-2) [30]. For the Fe/Ce/SiO_2-K, Cu catalyst, pores might have turned into cavities because the surface was still more rough than Fe/Zr/SiO_2-K,Cu. The surface of Fe/Zr/-SiO_2-K,Cu had small cracks due to capillary forces or high temperature in the calcination stage. The particle size for Fe/Ce/SiO_2-K,Cu was around 115 μm while it was 110 μm for Fe/Zr/SiO_2-K,Cu (Table 1).

The catalysts containing the Sasol support, Fe/Catalox-K,Cu and Fe/Dispal-K,Cu were predominantly spherical (Figs 4bc, 5bc) with some donuts (Figs 4a,5ab). The Catalox as a support had the same spherical shape as the catalyst according to the Sasol technical sheet. This suggests that, the NHSG method preserves the shape and structure of the original precursor and it is a non-invasive method. However, created colloidal structure still managed to hold the additional metal oxide on the surface. SEM-EDX indicated that iron particles formed few islands on the surface around the support. Al, Cu, and K are distributed relatively evenly (Supporting Document 5a). There are a few iron and potassium particles

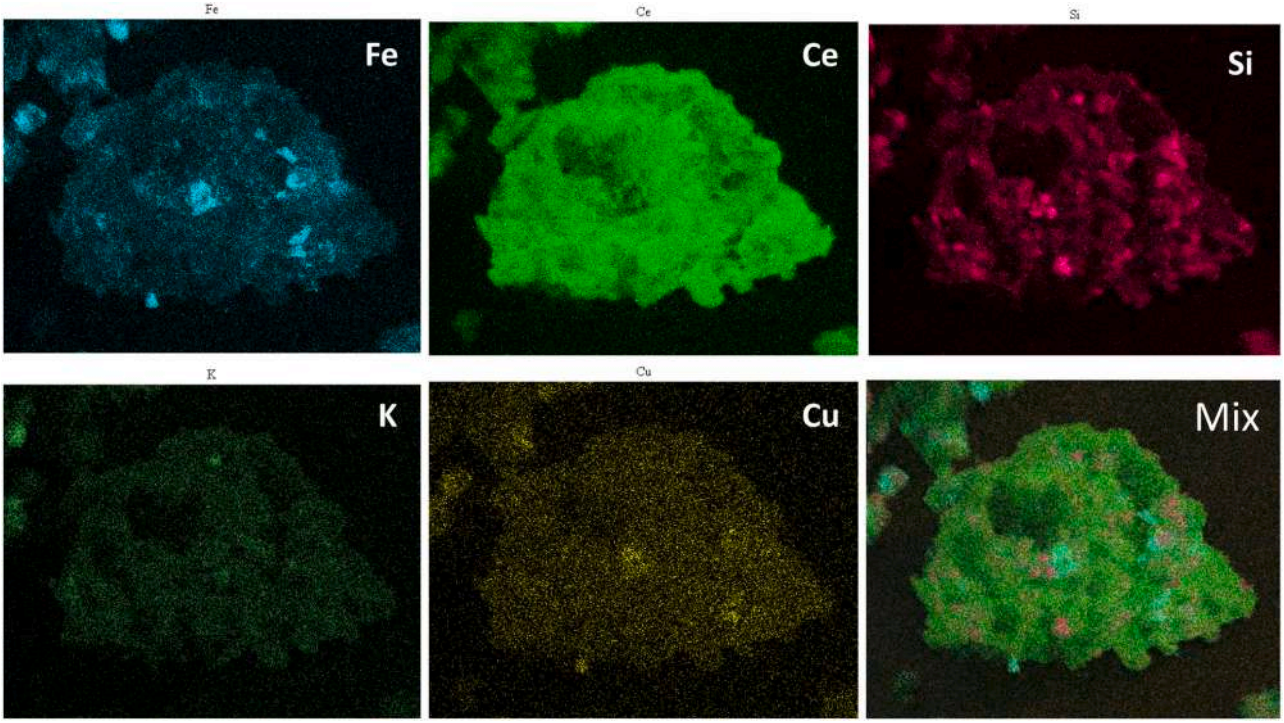

Fig. 1. Detailed SEM-EDX representation of Fe/Ce/SiO_2-K,Cu and mix of all the elements, x750 magnification, 10 μm scale.

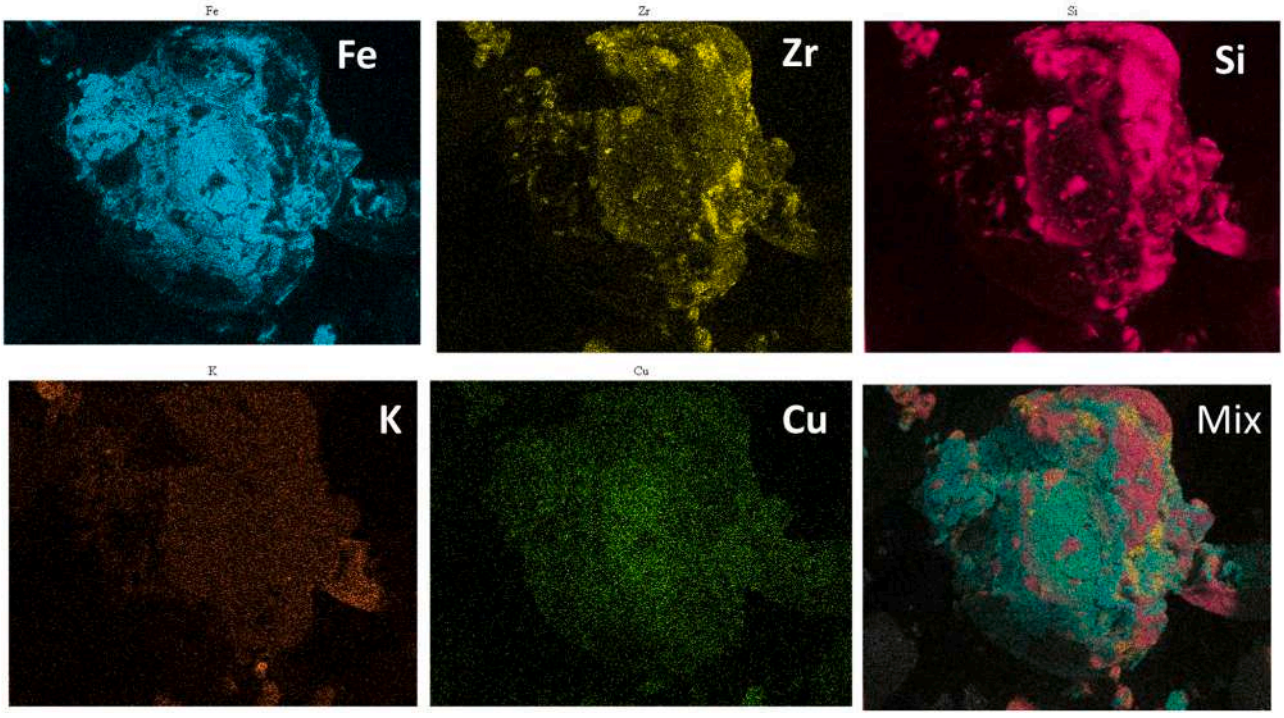

Fig. 2. Detailed SEM-EDX representation of Fe/Zr/SiO_2-K,Cu and mix of all the elements, x270 magnification, 10 μm scale.

located inside of voids. For the Dispal supported catalyst, the metal distribution is similar, however, the spot analysis indicated that Fe, K, and Cu weight percent average is 5% lower than the Catalox supported catalyst. The common detail about these both catalysts is that higher Al content on the catalyst surface compared to Si of metallosilicates. (Supporting Document 5ab)

The BET surface area of Fe/Ce/SiO_2-K,Cu and Fe/Zr/SiO_2-K,Cu were lower than the non-promoted catalysts: 24 $m^2\ g^{-1}$ for Fe/Ce/SiO_2-K,Cu and 204 $m^2\ g^{-1}$ for Fe/Zr/SiO_2-K,Cu for fresh catalysts (Table 1). The disparity in surface area between these two catalysts primarily stems from the impact of precursor used in the sol-gel method for synthesizing the supports. We synthesized the supports using the conventional sol-gel method, which utilizes water as a solvent. This method is influenced by factors such as the type of precursor, water content, pH of the solution, and temperature of the reaction [31–33]. Conventional sol-gel method (water as a solvent) used in the support synthesis is sensitive to the type

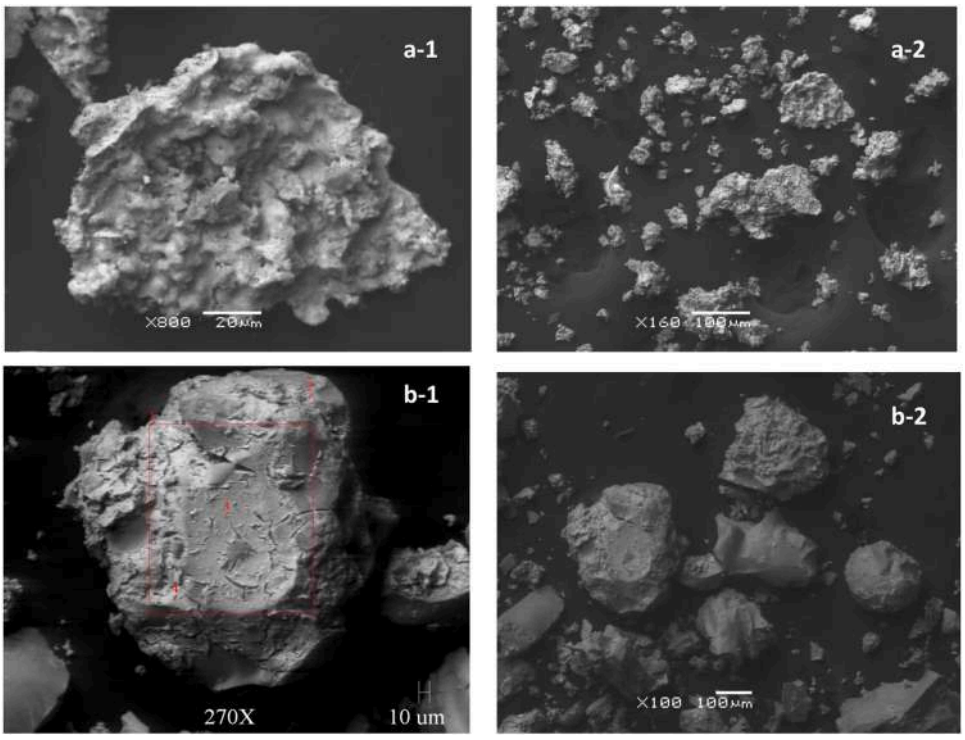

Fig. 3. The Scanning Electron Microscope Images of both Fe/Ce/SiO_2-K,Cu (a-1: x800 and a-2: x160 magnification) and Fe/Zr/SiO_2-K,Cu (b-1: x270 and b-2: x100 magnification).

Table 1
Different properties of iron supported catalysts.

Catalysts	Particle diameter (μm)	Average Pore diameter (nm)	Pore volume ($cm^3\ g^{-1}$)	Specific surface area ($m^2\ g^{-1}$)	d (Fe_2O_3) (nm)	d (Fe_3O_4) (nm)
Fe/Ce/SiO2-K,Cu	115	16	0.1	24	9	–
Fe/Zr/SiO2-K,Cu	110	4	0.1	204	2	–
Fe/Catalox-K,Cu	64	6	0.4	84	6	–
Fe/Dispal-K,Cu	50	6	1.0	150	–	3

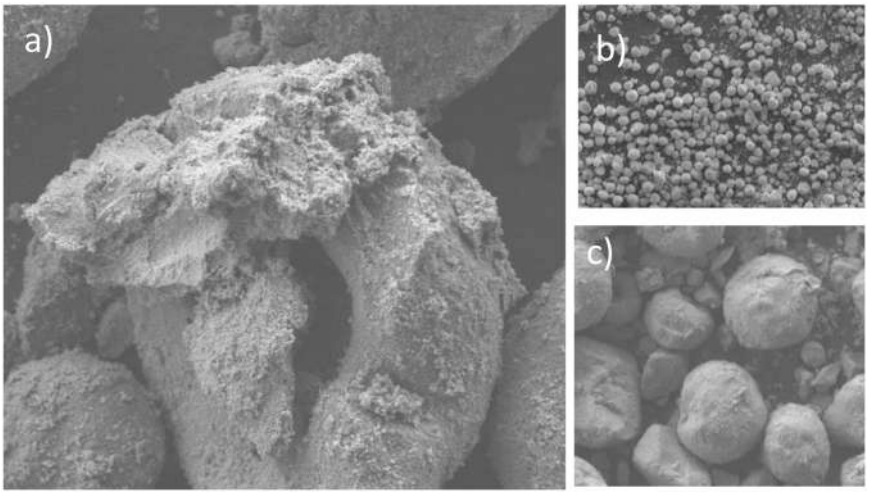

Fig. 4. SEM of Fe/Catalox-K,Cu (a) x1400, (b) x65 and (c) x1000 magnification.

of precursor due to different hydrolysis and condensation rates during the reaction. Apart from the precursor type, we prepared both supports simultaneously under the identical conditions. Despite having the same metal loading for the ammonium cerium nitrate and zirconium ethoxide precursors, the surface areas differed by an order of magnitude A similar conventional sol-gel method [34] also reported large differences in BET surface area of the supports: 42 $m^2\ g^{-1}$ for cerium silicate support and 366 $m^2\ g^{-1}$ for zirconium silicate support [17]. The influence of different precursors on surface area can also be observed in the referenced study, where the researchers synthesized Al, Ti, Zr, Ce, V, and Zr

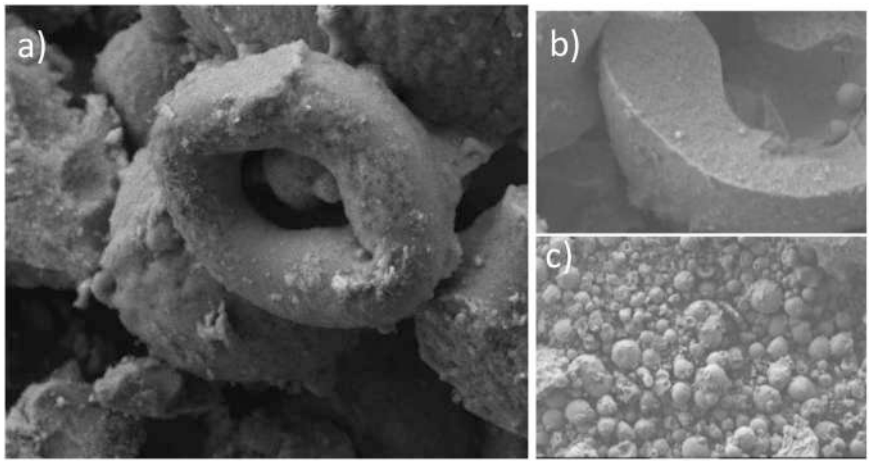

Fig. 5. SEM of Fe/Dispal-K,Cu (a) x3500 (b)x5000 (c) x250 magnification.

metallosilicates with cobalt as an active phase for FTS [34]. The surface area of these supports ranged from 16 m^2 g^{-1} (for vanadium silicate synthesized using ammonium metavanadate) to 627 m^2 g^{-1} (for titanium silicate synthesized using titanium n-butoxide). Moreover, the BET results from that study demonstrated a 217 m^2 g^{-1} difference in surface area between cerium silicate and zirconium silicate supports [34].

We measured the surface area for fresh catalyst and after 90 h reaction with syngas (H_2/CO=2) at 20 bar and 275 °C to (numerical range) 325 °C. Both Fe/Ce/SiO_2-K,Cu and Fe/Zr/SiO_2-K,Cu catalysts had a mesoporous structure, which was maintained after reaction. The nitrogen adsorption-desorption for Fe/Ce/SiO_2-K,Cu resembles Type III isotherms with a H3 hysteresis loop. This is typical of non-rigid aggregates of clay type, plate-like particles [35–37]. After reaction, the pores are narrower because of the carbon deposition (Fig. 6).

The isotherms of the fresh Fe/Zr/SiO_2-K,Cu resembles a H5 hysteresis loop of a Type IV adsorption-desorption isotherms, which is linked with partially open pore structures containing cylindrical mesopores (Fig. 6). After the reaction it had Type IV isotherms with a H2(a) hysteresis loop that is associated with bottle-neck looking pores characteristic of many silica gels, porous glasses, and mesoporous materials [37]. The interaction of gas through the partially open pores enlarges the mouth of the pores. This also explains why the pore size and BET surface area is larger after the reaction (207 m^2 g^{-1}). Since the zirconium silicate supported catalysts were less active, the carbon deposition on the pores could have less impact on the pore size as well. Pore size distribution demonstrated that most pore sizes are in between 2 nm to (numerical range) 5 nm indicating mesoporous structure with 44% and 84% for cerium and zirconium supported iron catalyst, respectively

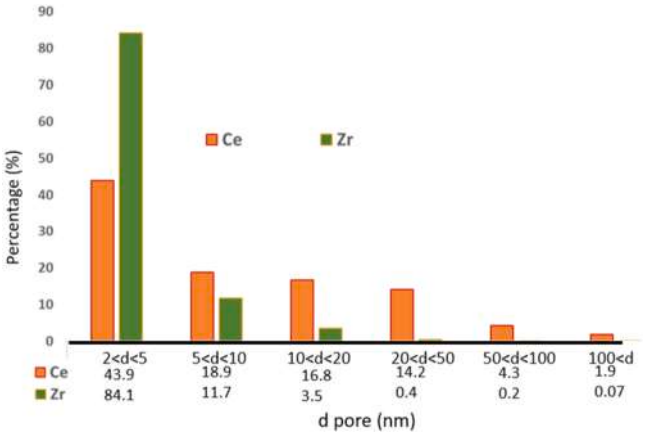

Fig. 7. The pore size distributions from d < 2 nm and 100 nm < d for Fe/Ce/SiO_2-K,Cu-orange andFe/Zr/SiO_2-K,Cu-green.

(Fig. 7).

The BET surface area was 84 m^2 g^{-1} for the Catalox supported catalyst and 150 m^2 g^{-1} for the Dispal supported catalyst. They both had about the same pore size (6 nm) and a mesoporous structure. Based on their pore size distribution, the highest percentage is in between 2 nm to (numerical range) 5 nm for sasol supported catalysts as well with 64% and 56% for Fe/Dispal-K,Cu and Fe/Catalox-K,Cu respectively (Fig. 8). The particle size for Fe/Catalox-K,Cu was around 64 μm while it was 50

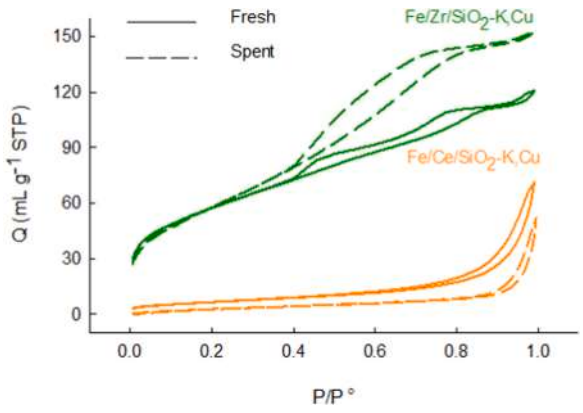

Fig. 6. BET adsorption-desorption isotherms of both Fe/Ce/SiO_2-K,Cu and Fe/Zr/SiO_2-K,Cu fresh and spent.

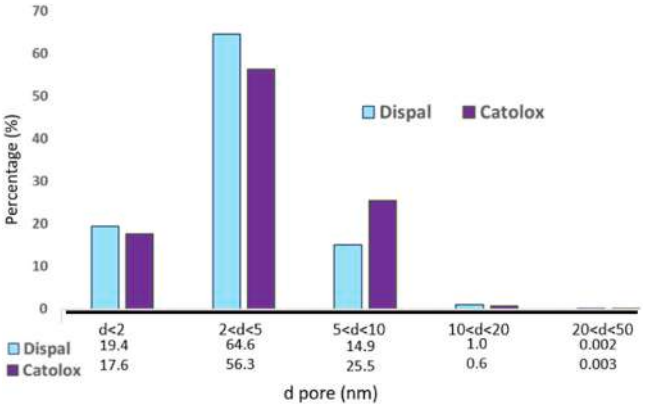

Fig. 8. The pore size distributions from d < 2 nm and 100 nm < d for Fe/Catalox-K,Cu-purple, Fe/Dispal-K,Cu-turquoise.

μm for Fe/Dispal-K,Cu (Table 1).

The Fe/Catalox-K,Cu follows a Type V adsoption-desorption isotherm which was similar to zirconium silicate supported catalysts that indicate molecular clustering, partially-open ordered pores (Fig. 9). This is common for mesoporous structures, mixed oxides, and xerogels. The hysteresis loops were close to H2(a)—bottle neck structured pores. H2 type loops are common for silicate/aluminosilicate pore structures. The Fe/Dispal-K,Cu catalyst had Type III isotherm and similar to Type V as well with the H3 type hysteresis loop. For the H3 loop, the pore structure is ill defined [37−39].

The XRD diffractograms of the samples (Fig. 10 and Fig. 11) were interpreted with both EXPO2014 and the Match! software. Since both metallosilicate supported catalysts include multiple metal oxides, the patterns overlap [40]. The Match software computes and matches the peaks along with the amounts and phases of the elements based on COD (Crystallography Open Database) where EXPO2014 solves crystal structures (if there is any) by powder diffraction data by using reciprocal as well as direct space methods. According to the software, the Fe/Ce/SiO_2-K,Cu identified Fe_2O_3-hematite as the Fe phase and the peak values are confirmed by other studies [41–44]. The software identified SiO_2 and CeO_2 along with K_2O and the tenorite form of CuO (Fig. 10). The Fe/Zr/SiO_2-K,Cu displayed peaks characteristic of Fe_2O_3 in hematite form [43,44]. The analyses were based on ICDD and COD, which identified in its crystalline structure, the Fe/Zr/SiO_2-K,Cu catalyst has the paramelaconite form of Cu_4O_3 along with ortho I phase of ZrO_2 (Fig. 11). In addition to this, there are SiO_2 peaks in mutinaite phase. Since the software assigned a value of 76% to SiO_2, it is likely that the Fe/Zr/SiO_2-K,Cu is amorphous. This is further evidenced by the presence of a “hump” on the baseline of its diffractograms [45].

We observed some residual structures of $CeSiO_2$ and $ZrSiO_4$ originated from the support material for Fe/Ce/SiO_2-K,Cu and Fe/Zr/SiO_2-K,Cu, respectively. This also suggests that we successfully synthesized cerium silicate and zirconium silicate supports separately. EXPO2014 software analysis also confirmed this finding. From the XRD results of Fe/Ce/SiO_2-K,Cu, we differentiate the neat peaks which represents crystallinity. EXPO2014 was able to form a crystalline structure for Fe/Ce/SiO_2-K,Cu (Fig. 12), unlike for Fe/Zr/SiO_2-K,Cu due to its amorphous structure [46–48,44,49,43,50,51]

For the Catalox supported catalyst, the Fe_2O_3-hematite appeared as the active phase while for the Dispal supported catalyst, the iron phase was Fe_3O_4 based on the XRD results. However, for the Fe/Catalox-K,Cu, a small trace of Fe_3O_4 was also present. In Fe/Catalox-K,Cu, the XRD has a K_2O peak and we were also able to identify small percentage of $AlKO_2$ (Fig. 13 and Fig. 14), which suggests a bond bridge between the support and the promoter. The Cu_4O_3 was tetragonal and Al_2O_3 in theta form. The Fe/Dispal-K,Cu consisted of iron oxide as magnetite, Fe_3O_4, and

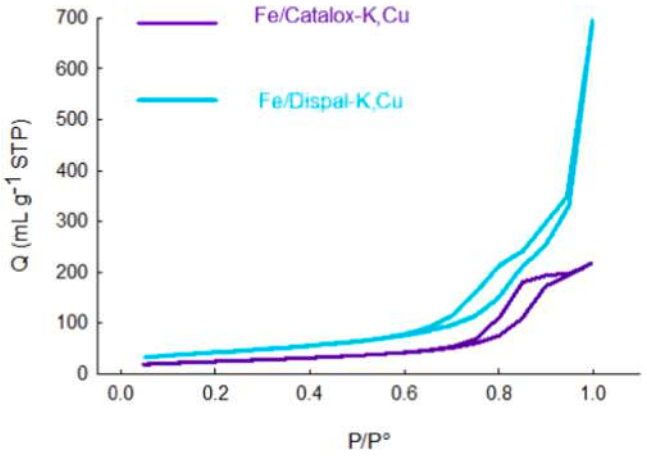

Fig. 9. BET adsorption-desorption isotherms of both Fe/Catalox-K,Cu and Fe/Dispal-K,Cu.

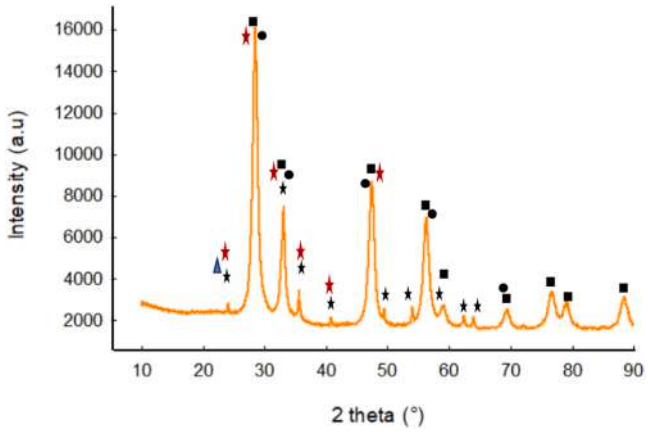

Fig. 10. X-Ray Diffractograms of both Fe/Ce/SiO_2-K,Cu black star-Fe_2O_3, black square CeO_2, black circle - CuO, red star-K_2O, blue circle- SiO_2.

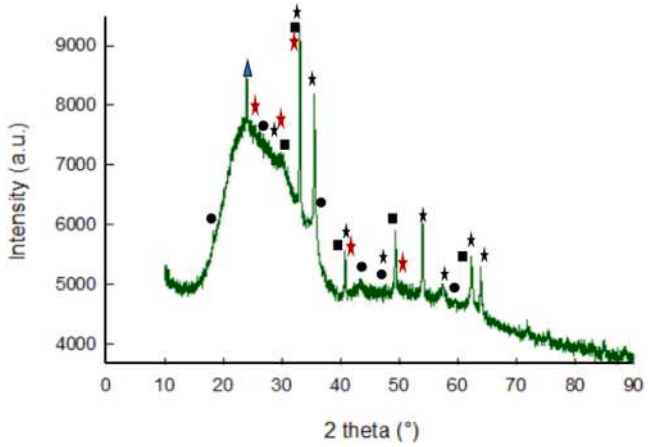

Fig. 11. X-Ray Diffractograms of both Fe/Zr/SiO_2-K,Cu black star-Fe_2O_3, black square ZrO_2, black circle - Cu_3O_4, red star-K_2O, blue triangle- SiO_2.

Al_2O_3, CuO in tenorite form, with a trace of KO_3. However, the peaks in Dispal supported catalyst was not as sharp as the Catalox supported catalyst, which could be the reason why the latter was more stable and active. This suggests that Fe/Dispal-K,Cu consists of an amorphous aluminum oxide structure that is similar to zirconium silicate supported catalyst (Supporting Figure 1–4). Especially iron crystallite size correlate with CO conversion and C_{5+} product selectivity. In our case, iron crystallites between 6 nm to (numerical range) 10 nm are more active and produce a heavier hydrocarbons (Table 1). The crystallite size smaller than 6 nm to (numerical range) 12 nm demonstrates lower catalytic activity, higher methane and CO_2 selectivity and lower the chain growth. [52–54].

Both catalysts have mixed oxides which appears at the same 2θ°. For example, Fe_2O_3 [43], Fe_3O_4 [55], K_2O [56], CuO[57,58], Al_2O_3 [59] and Cu_4O_3 [60] has at least 2 peaks assigned to this crystal structure in between 30 and 40 2θ°. Therefore, it is challenging to distinguish the peaks and this is why some peaks appear merged. Also similar to metallosilicates, EXPO2014 identified an ordered crystalline form for Catalox supported catalyst but not for the Dispal supported one (Fig. 15). Further analysis performed by XPS confirms the oxidation state or chemical state of the metallic elements.

The surface of the sample was gently etched using Ar+ cluster ions at 4 keV for 1000 atoms clusters to remove adventitious carbon contaminants. All spectra are charge corrected to the remaining C1s peak at a binding energy (BE) of 284.8 eV The survey spectra obtained from the metallosilicate supported catalysts (Fig. 16) displayed the presence of

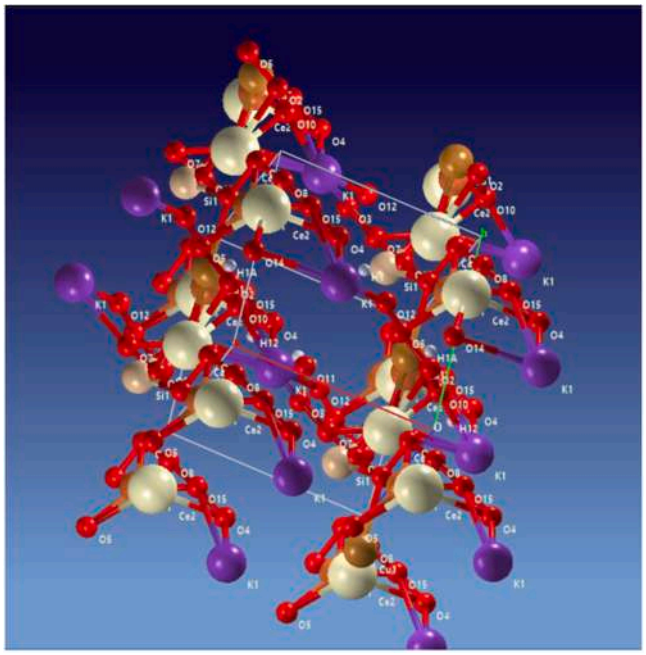

Fig. 12. Crystalline structure of Fe/Ce/SiO_2-K,Cu according to analysis of XRD data by the EXPO2014 software.

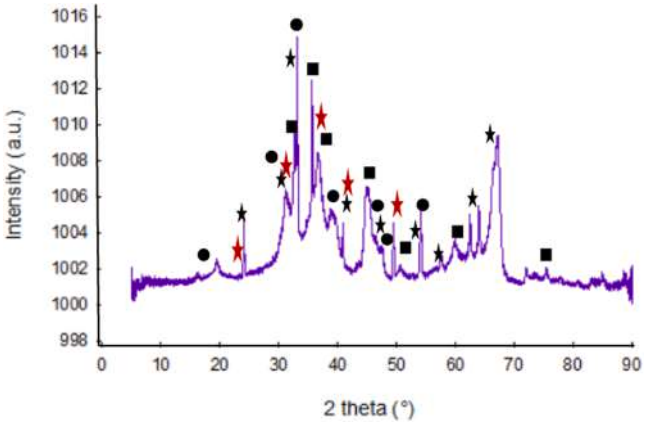

Fig. 13. XRD of Fe/Catalox-K,Cu and black star—Fe_2O_3, black square Al_2O_3, black circle—Cu_3O_4, red star-K_2O.

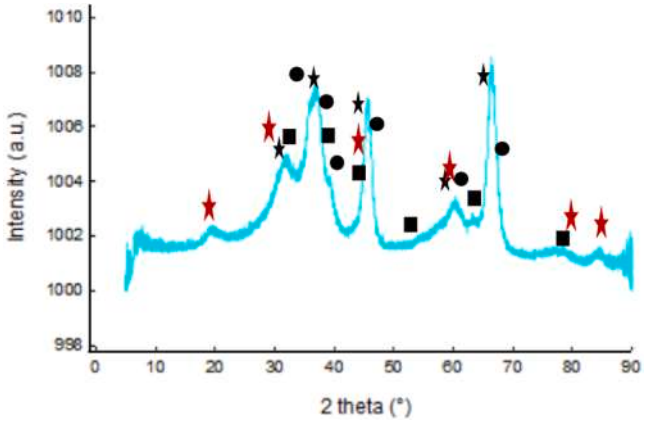

Fig. 14. X-Ray Diffraction of both Fe/Dispal-K,Cu and black star—Fe_3O_4, black square Al_2O_3, black circle—CuO, red star-KO_3.

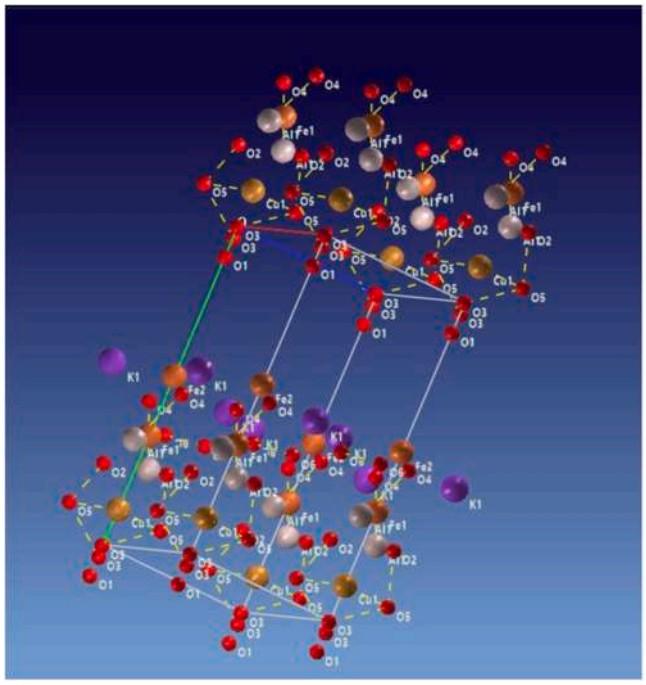

Fig. 15. Crystalline structure of Fe/Catalox-K,Cu according to analysis of XRD data by the EXPO2014 software.

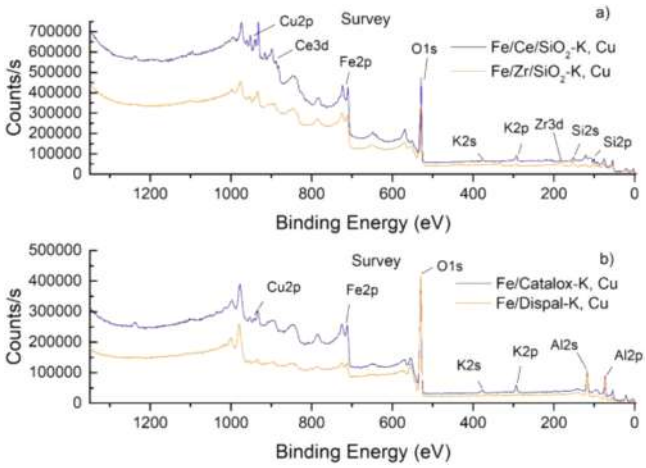

Fig. 16. XPS survey spectra for catalysts a) Fe/Ce/SiO_2-K,Cu (blue line) and Fe/Zr/SiO_2-K,Cu (orange line), and b) Fe/Catalox-K,Cu (blue line) and Fe/Dispal-K,Cu (orange line).

elements Si, K, O, Fe, and Cu, also the corresponding metallic element, Ce or Zr for Fe/Ce/SiO_2-K,Cu and Fe/Zr/SiO_2-K,Cu catalysts, respectively with the elemental quantification (Table 2). The lower Si

Table 2
Elemental quantification table from survey spectra for metallosilicate catalysts.

Element and orbital	BE (eV)	Relative atomic %	
		Fe/Ce/SiO2-K,Cu	Fe/Zr/SiO2-K,Cu
Si2p	102.4	7.1	17.9
Zr3d	182.7	—	1.8
K2p	294.4	3.1	1.7
O1s	530.9	74.1	68.8
Fe2p3/2	711.4	8.5	7.1
Ce3d5/2	883.2	1.3	—
Cu2p3/2	933.8	6	2.8

concentration and higher concentrations of K, Fe, and Cu observed on the surface of Fe/Ce/SiO_2-K,Cu compared to Fe/Zr/SiO_2-K,Cu suggests an increased metal distribution on the SiO_2 support in the Fe/Ce/SiO_2-K, Cu compared to the latter catalyst (Table 3).

The high resolution XPS spectra for both Fe/Ce/SiO_2-K,Cu and Fe/Zr/SiO_2-K, Cu(Fig. 17) indicated a Si2s peak centered at BE=153.4 eV consistent with Si in silicates, and K2p3/2 (K2p1/2) peak at BE=293.6 (295.4) eV, consistent with K bonding to oxygen atoms. The highest intensity of the Fe2p3/2 peak was observed at BE = 711.4 eV consistent with a dominant presence of Fe in Fe(III) oxide. Fe/Ce/SiO_2-K, Cu also indicated a well-defined Fe2p3/2 shake up peak at BE = 719.2 eV as expected in Fe(III) oxides. The Fe/Zr/SiO_2-K,Cu exhibited a noticeable broadening of the Fe2p3/2 peak towards 708.0 eV, suggesting the existence of a minor concentration of Fe(II) oxide, potentially linked to the presence of magnetite in the sample.

For both catalysts, the Cu2p3/2 peak had the highest intensity at BE = 934.0 eV and indicated intense shake up satellite ranging from 940 eV to (numerical range) 945 eV consistent with Cu in Cu(II) oxide (CuO) [61]. In the Fe/Ce/SiO_2-K, Cu catalyst, the Ce3d spectrum displayed spin-orbit components Ce3d5/2 and Ce3d3/2 separated by 16.0 eV. Each of these components further splits into three multiplet components, consistent with the presence of CeO_2. The catalyst Fe/Zr/SiO_2-K,Cu: Zr3d was curve-fit using two spin-orbit split ($\triangle$ = 2.4 eV) doublet Lorentzian/Gaussian (L/G) peaks of fixed relative intensity 2:3 for Zr3d3/2: Zr3d5/2 with constant full-width-half-maximum (FWHM) and L/G ratio. Components of Zr3d5/2 appearing at BE = 181.9 eV and BE = 183.2 eV could be related to the presence of ZrO2 and ZrSiO4.

Both Sasol supported catalysts demonstrate similar concentrations of Al and O as a percentage in the sample (Fig. 16-b) (Table 4Table 5). The concentration of Fe relative to Al was similar. Concentrations of K and Cu were significantly higher on the surface of Catalox compared to Dispal. The low concentrations of Fe, K and Cu relative to aluminum oxide found for both catalysts indicated that the metals were more homogeneously distributed or embedded in the catalyst body compared to the silicate supported catalysts for which had higher surface concentrations relative to Si. For both cerium and zirconium silicate supported catalysts, the SiO_2 was located below the surface while the other elements were at the surface (Fig. 18). These findings were confirmed with SEM-EDS results as well, which helped us deduct the catalyst structure for both iron metallosilicates and iron aluminum oxides [62] (Fig. 18). (Fig. 1, Fig. 2, Supporting Document 5-a, 5-b)

The high resolution spectra for Sasol-supported catalysts (Fig. 19) indicated Al2s at BE = 118.0 eV, which is consistent with Al in alumina. The broader peak for Dispal could be indicative of a more disordered structure for this support. K2p3/2 was observed at BE = 293.0 eV, which is consistent with K in metallosilicate-supported catalysts. (Ref. NIST XPS database SRD 20). Fe2p had a very similar shape for both Catalox and Dispal supported catalysts, consistent with Fe_2O_3. However, maximum intensity of Fe2p3/2 was found at BE = 712.0 eV for Fe/Catalox-K,Cu while it was at BE = 713.0 eV for Fe/Dispal-K,Cu. The shift in binding energy could be due to differences in oxide structure or crystallinity. Since XRD indicated that Fe_3O_4 as the dominant iron phase in Fe/Dispal-K,Cu with mostly amorphous structure compared to Fe/Catalox-K,Cu, this is a strong possibility. A similar effect was observed in the Cu2p spectra where the lineshapes are consistent with Cu in Cu(II) oxide, but the binding energy at which the Cu2p3/2 peaks are observed, 934.4 eV and 935.5 eV for the Fe/Catalox-K,Cu and Fe/Dispal-K,Cu respectively, are higher than generally observed.

Table 3
Metal to Si concentration ratios for metallosilicate catalysts.

Species concentration ratio	Fe/Ce/SiO2-K,Cu	Fe/Zr/SiO2-K,Cu
Zr or Ce/Si	0.2	0.1
K/Si	0.4	0.1
Fe/Si	1.2	0.4
Cu/Si	0.9	0.2

3.2. FT Reaction

The Fischer Tropsch reaction forms hydrocarbons ranging from C_1 to C_{100}, carbon dioxide, and water. We report CO conversion, and selectivity of CO_2, CH_4, light hydrocarbons from C_2 to C_6 and heavy hydrocarbons, C_{7+}. After the catalyst was activated at 350 ˚C for 4 h, the reactor was set at 200 ˚C and ramped every 24 h (220 ˚C, 250 ˚C, 275 ˚C, 300 ˚C, 325 ˚C, typically). All the tests were conducted at 20 bar, 200 ˚C to (numerical range) 350 ˚C, and a 2:1 H_2/CO molar ratio. Experimental data were recorded after reaching steady state. The CO conversion for Fe/Ce/SiO_2-K,Cu catalysts increased from 13% at 200 ˚C, to 48% at 275 ˚C, and finally 86% at 325 ˚C. (Fig. 20). For the Fe/Zr/SiO2-K,Cu conversion was 10% at 200 ˚C, and increased to 40% at 275 ˚C and to 76% at 325 ˚C. The overall CO conversion for Fe/Ce/SiO_2-K,Cu is higher than the Fe/Zr/SiO_2-K,Cu catalyst but they both follow the same trend with temperature. At a reaction temperature of 350 ˚C for 30 h, non promoted Fe/Ce/SiO_2 and Fe/Zr/SiO_2 catalysts achieved conversion of only 68% and 52%,respectively [17].

The selectivity of both catalysts followed the same trend with temperature (Fig. 21) For the promoted Fe/Ce/SiO_2-K,Cu, CH_4 selectivity is the lowest, starting at around 1% at 220 ˚C and then increasing, as expected, reaching a maximum of 13% at 325 ˚C. The non-promoted counterparts on the other hand, had the lowest methane selectivity at 250 ˚C at 6% but reached 15% at 270 ˚C and 27% at 300 ˚C. The Fe/Zr/SiO_2-K,Cu overall CH_4 selectivity is lower compared to the non-promoted version. These results suggest that the promotion of the Fe/Ce/SiO_2-K,Cu and Fe/Zr/SiO_2-K,Cu decreases methane selectivity compared to their non-promoted counterparts.

Overall selectivity towards CO_2 was higher compared to the non-promoted version. For the Fe/Ce/SiO_2-K,Cu, CO_2 was 6% from 200 ˚C to (numerical range) 220 ˚C, and averaged 22% between 250 ˚C to (numerical range) 275 ˚C, and 44% from 300 ˚C to (numerical range) 325 ˚C. The promoted iron zirconium silicate also had a similar trend; the average CO_2 selectivity was 12% from 200 ˚C to (numerical range) 220 ˚C, 18% between 250 ˚C to (numerical range) 275 ˚C and 36% from 300 ˚C to (numerical range) 325 ˚C. Since the CH_4 selectivity was lower but CO_2 selectivity was higher in comparison to the non promoted catalyst, this indicates that the selectivity shifted from methane to carbon dioxide. K, is known to produce CO_2 when the loading is above a certain threshold but varies from catalyst to catalyst. The K loading improves both FTS and Water Gas Shift (WGS) activity but increasing the loading favors WGS instead and produces CO_2 [13,15,63,64]. Therefore, adjusting the K loading could decrease the CO_2 selectivity. Double promotion with Cu improves the stability and FTS activity significantly [13,65–67].

The light hydrocarbon C_{7-} selectivity for Fe/Ce/SiO_2-K,Cu was quite low compared to the non promoted catalyst up to 275 ˚C, after which it increased to 24% and was invariant while, the non promoted Fe/Ce/SiO_2 decreased to ~ 18%. The C_{7-} selectivity of Fe/Zr/SiO_2-K,Cu was highest at 29% at 325 ˚C. On the other hand, the C_{7+} selectivity reached maximum of 83% at 220 ˚C for Fe/Ce/SiO_2-K,Cu and for Fe/Zr/SiO_2-K, Cu, it was 58% at 220 ˚C. The C_{7+} selectivity decreased as the temperature increased after this point. Adding promoter also increases the CO chemisorption, which explains the shift of C_{7-} to C_{7+} [68].

The analytical data account for the difference in catalytic performance of metallosilicate supported iron catalysts. The SEM-EDX demonstrated that the elements are distributed more homogeneously for Fe/Ce/SiO_2-K,Cu compared to the Fe/Zr/SiO_2- K,Cu. In the latter case, metal agglomerates (islands) formed. A homogeneous distribution facilitates superior catalytic activity for Fischer Tropsch catalyst because it promotes the contact of the metal oxides with the reactant gases [69,70]. Normally, higher BET surface area correlates with improved performance. However, for the Fe/Ce/SiO_2-K,Cu the BET surface area is much lower than the Fe/Zr/SiO_2-K,Cu catalyst. Therefore, the surface

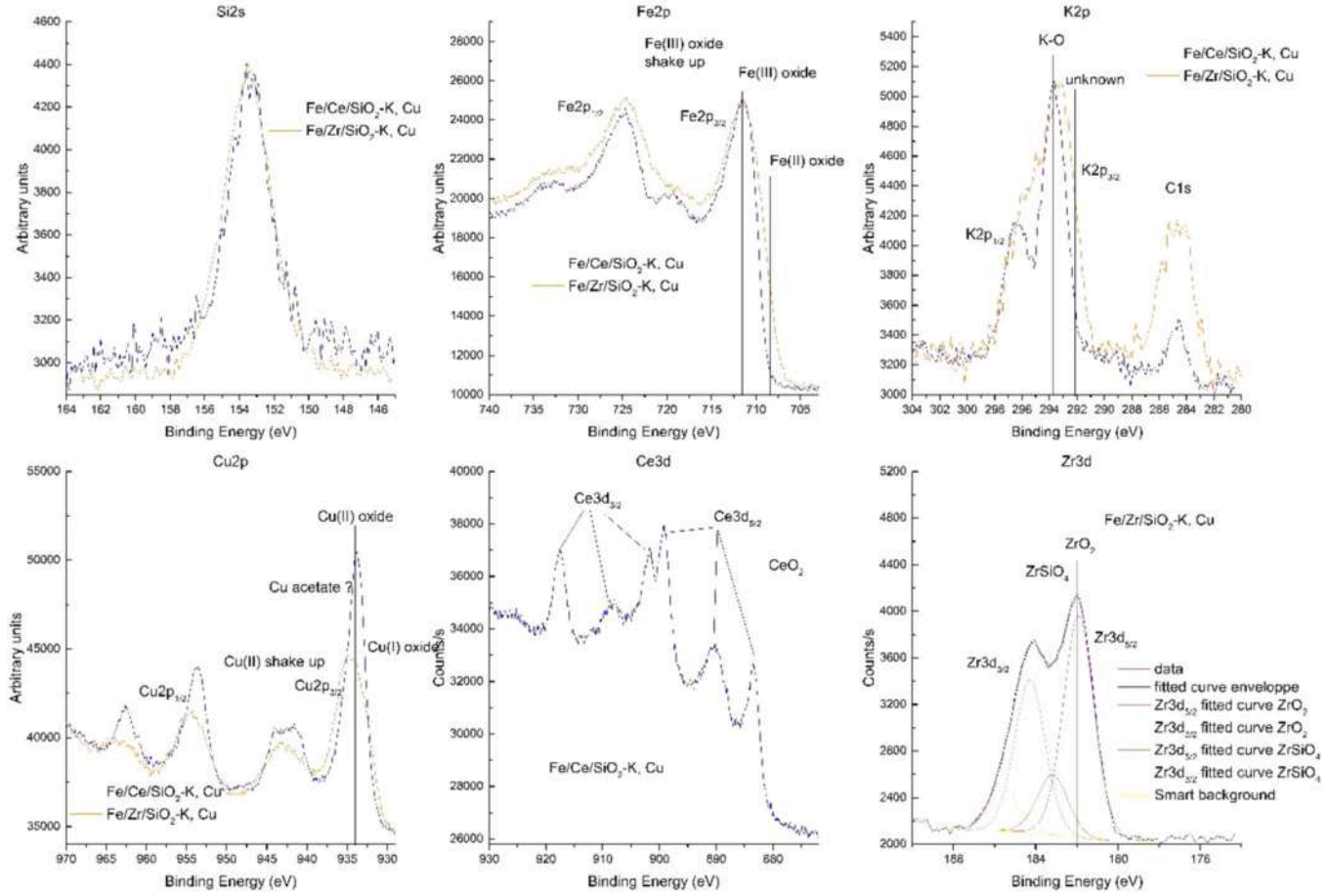

Fig. 17. High resolution spectra for catalysts a) Fe/Ce/SiO_2-K,Cu (blue line) and Fe/Zr/SiO_2-K,Cu (orange line). The intensity for spectra Si2s, Fe2p, K2p, and Cu2p was normalized to maximum intensity to ease comparison of spectral shape.

Table 4
Elemental quantification table from survey spectra for aluminum oxide-supported catalysts.

Element and orbital	BE (eV)	Relative atomic %	
		Fe/Catalox-K,Cu	Fe/Dispal-K,Cu
Al2p	74.8	34.3	36.1
K2p	295.1	2.2	0.3
O1s	531.9	58.6	60.1
Fe2p3/2	712.4	3.7	3
Cu2p1/2*	955	1.2	0.5

Table 5
Table of metals to Al concentration ratios for aluminum oxide supported catalysts.

Species concentration ratio	Fe/Catalox-K,Cu	Fe/Dispal-K,Cu
K/Al	0.06	0.01
Fe/Al	0.1	0.1
Cu/Al	0.03	0.01

area by itself is insufficient to predict the catalyst performance. BET-BJH indicated that both structures were mesoporous but the pore size was larger for the Fe/Ce/SiO_2-K,Cu (15 nm) compared to Fe/Zr/SiO_2-K,Cu (4 nm). The small pore sizes limits the diffusion of the reactants and the products, which lowers catalytic activity. Larger pore size improves the diffusion of reactants and limits the re-adsorption of olefins, which produces heavy hydrocarbons because it induces the production of long carbon chain [53][71][72][73]. Also, XRD indicated that the crystallinity was higher for the cerium silicate supported catalyst, while it was amorphous for the zirconium silicate supported catalyst. The lack of crystallinity might account for the lower catalytic activity of Fe/Zr/SiO_2-K,Cu [74].

The stability of metallosilicates and performance of the catalyst differs based on the active metal. For example, 0.2 g g^{-1} cobalt was supported on Al, Zr, V and Ti silicates and tested at 230 ˚C and 1 MPa. The highest conversion was 60% with Ti silicate support with 83% selectivity towards C_{5+} [75]. More recently, another study tested cobalt metallosilicates [34] at 220 ˚C, 1.83 MPa for almost 100 h. The CO_2 selectivity was lower (0.3% for Co/ZrTUD-1 and 4.5% for Co/CeTUD-1) in comparison to iron metallosilicates. However, the promoted iron catalysts exhibit a much lower CH_4 selectivity, even at 275 ˚C for Fe/Zr/SiO_2-K,Cu and 300 ˚C for Fe/Ce/SiO_2-K,Cu (both ~ 7% selectivity). The C_{5+} selectivity is almost the same for both iron and cobalt cerium silicate catalysts (~ 90%) at 220 ˚C. However, the zirconium silicate support was slightly more stable and the C_{5+} selectivity with cobalt as an active metal was higher, 88.2%, compared to iron at 66%. Furthermore, comparing the Co versus Fe metallosilicates at 220 ˚C is only valid for the first 6 h since our experiments directed at higher temperature and the catalyst activity changes after temperature increase [34].

We synthesized two additional iron catalysts using commercial Sasol supports, Catalox and Dispal. The CO conversion for the Catalox-supported catalyst reached 88% at 325 ˚C while it was 77% for the Dispal-supported catalyst (Fig. 22). While the CO conversion constantly increased with temperature for metallosilicate-supported iron catalysts, the catalysts containing the Sasol supporting materials depended less on temperature.

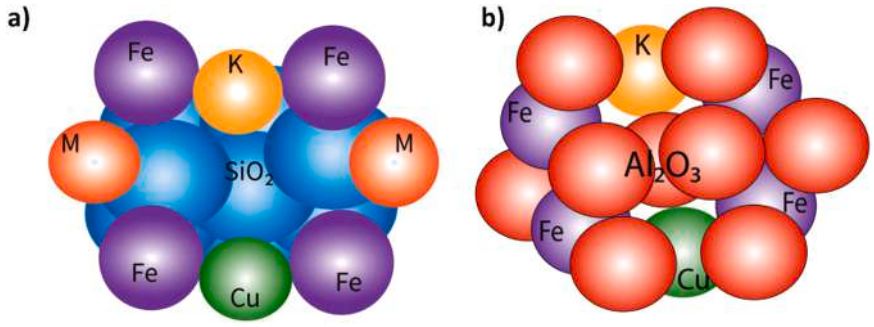

Fig. 18. Schematic representation of a) metallosilicate supported and b) aluminum oxide supported iron catalysts.

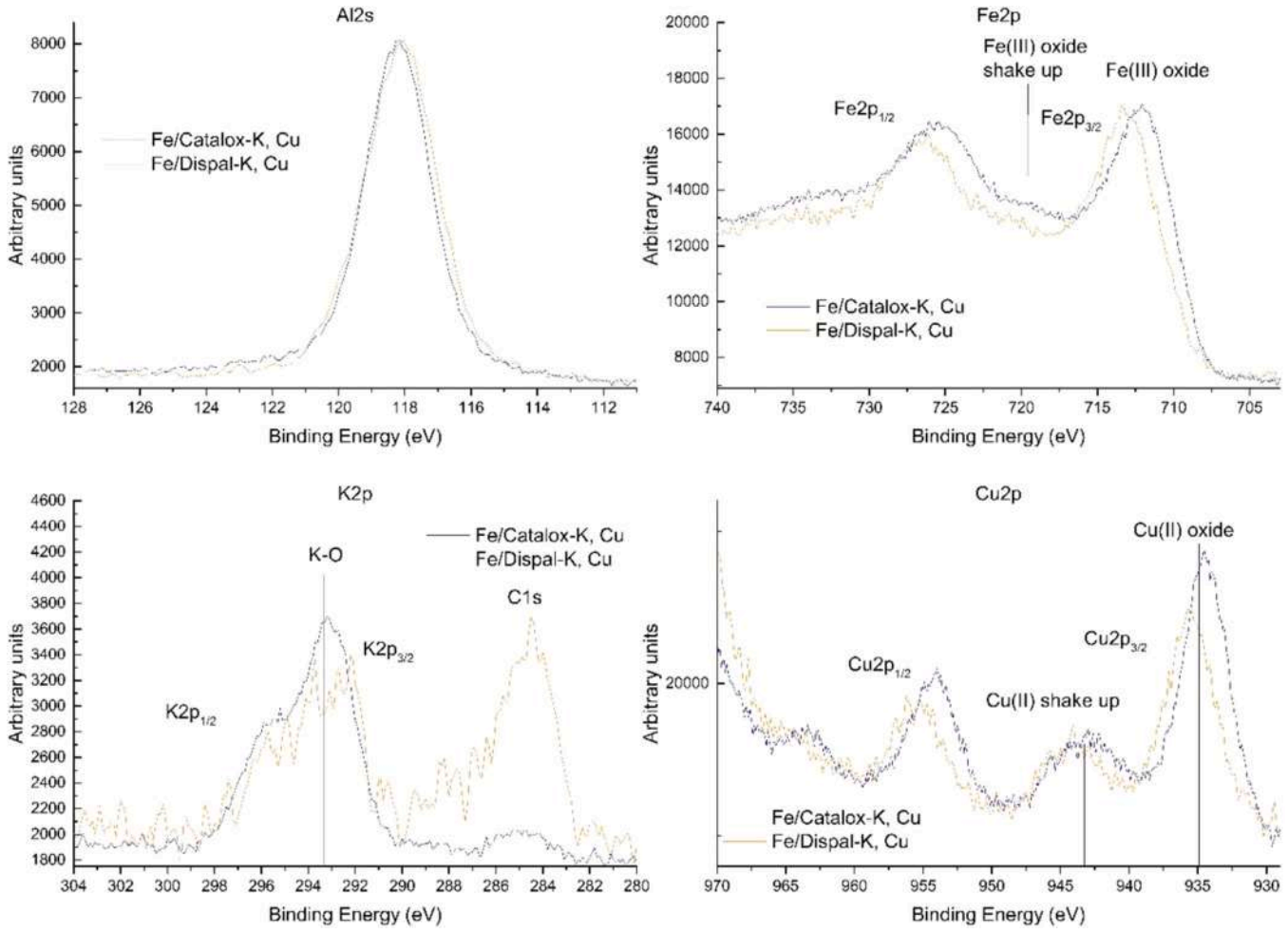

Fig. 19. High resolution spectra for catalysts Fe/Catalox-K,Cu (blue) and Fe/Dispal-K, Cu (orange). Spectral intensity was normalized to maximum intensity to ease comparison of spectral shape.

The average C_{7+} selectivity for the Catalox-supported catalysts was 64% at 275 ˚C (Table 6), and further dropped to 22% at 300 ˚C. However, as the temperature increased to 325 ˚C, the C_{7+} selectivity began to rise again reaching 47%. The Dispal-supported catalyst behaved similarly but with lower C_{7+} selectivity at each temperature (57%, 17% and 37% on average from 275 ˚C to (numerical range) 325 ˚C, respectively) (Table 6). For Fe/Catalox-K,Cu, the average CH_4 selectivity was 2%, 7% and 8% from 275 ˚C to (numerical range) 325 ˚C in order. The methane selectivity remained similar even as the temperature increased beyond 300 ˚C. For the Fe/Dispal-K,Cu, the methane selectivity was relatively higher, 4%, 9%, 11% from 275 ˚C to (numerical range) 325 ˚C. Although the methane production was similar for both catalysts up to 300 ˚C, it increased further as the temperature rose to 325 ˚C for Fe/Dispal-K,Cu. This implies that the catalyst may be susceptible to deactivation if the reaction time was extended at 325 ˚C.

Sasol-supported catalysts showed the highest selectivity for light hydrocarbons (C2-C6) at 300 ˚C (28% to (numerical range) 29%), but this temperature also resulted in high CO_2 selectivity (43% to (numerical range) 46%)(Table 6). Increasing the temperature to 325 ˚C decreased the CO_2 selectivity for both catalysts (3%, 5% difference, relatively). In summary, raising the temperature from 300˚C to (numerical range) 325˚C shifted the product range towards C_{7+} while methane selectivity remained relatively constant (for Fe/Catalox-K,Cu, while for Fe/Dispal-K,Cu methane selectivity increasesd) and CO_2 selectivity decreased.

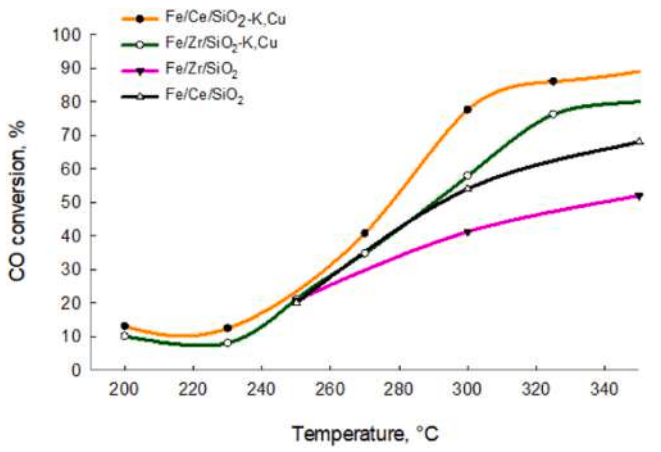

Fig. 20. Change in CO conversion with temperature, for Fe/Ce/SiO_2-K,Cu and Fe/Zr/SiO_2-K,Cu with their non promoted versions of each catalysts [17].

The alpha values based on the hydrocarbon distribution were 0.80, 0.76, 0.66 and 0.60 for Fe/Catalox-K,Cu, Fe/Dispal-K,Cu, Fe/Ce/SiO2-K,Cu and Fe/Zr/SiO2-K,Cu, respectively (Fig. 23). ASF predicts the product distribution based on the calculated alpha values (Fig. 24)[76]. The weight percentages of $C_5 - C_{11}$ are 42%, 45%, 40% and 30% while $C_{12} - C_{18}$ distribution is 22%, 12%,22%, 9% and 2% for Fe/Catalox-K, Cu, Fe/Dispal-K,Cu, Fe/Ce/SiO_2-K,Cu and Fe/Zr/SiO_2-K,Cu, respectively. The methane percentages for all the catalysts fit with the CH_4 selectivities we found. However, $C_2 - C_4$ selectivities for iron metallosilicates were lower around 15% compared to the predictions of ASF.

The nature of the support has a significant impact on the dispersion, reducibility, acidity and catalytic activity [77]. While there are no previous studies comparing metallosilicate with Al_2O_3, we can still draw some conclusions based on studies comparing SiO_2 and Al_2O_3. For example, one study found that alumina-supported catalysts form $FeAl_2O_4$, which stabilizes the structure more than silica-supported

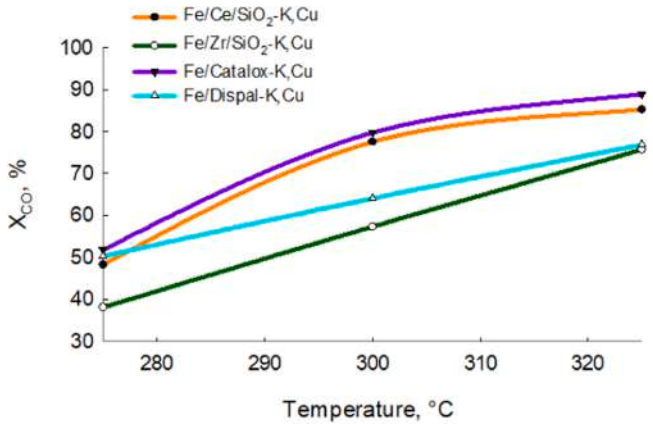

Fig. 22. The conversion of CO conversion vs temperature for of promoted Sasol supported and Metallosilicate supported iron catalysts.

Table 6
Selectivities of Fe/Catalox-K,Cu and Fe/Dispal-K,Cu.

	T (°C)	S_{CO2}	S_{C7-}	S_{C7+}	S_{CH4}
Fe/Catalox-K,Cu	275	20	14	64	2
	300	43	28	22	7
	325	35	10	47	8
Fe/Dispal-K,Cu	275	24	15	57	4
	300	46	29	17	9
	325	41	11	37	11

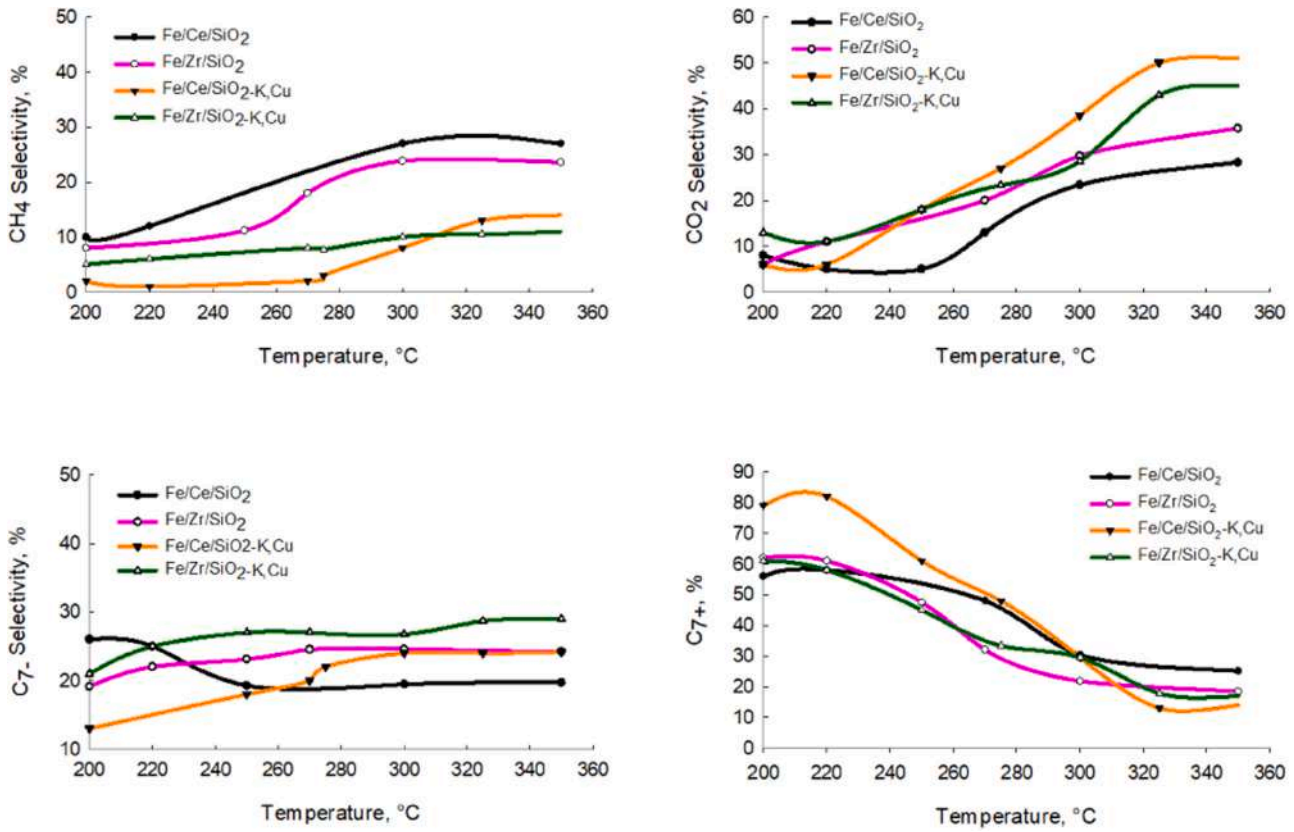

Fig. 21. CH_4, CO_2, C_{7-} selectivity and C_{7+} for unpromoted Fe/Ce/SiO_2 and Fe/Zr/SiO_2 vs Fe/Ce/SiO_2-K,Cu and Fe/Zr/SiO_2-K,Cu.

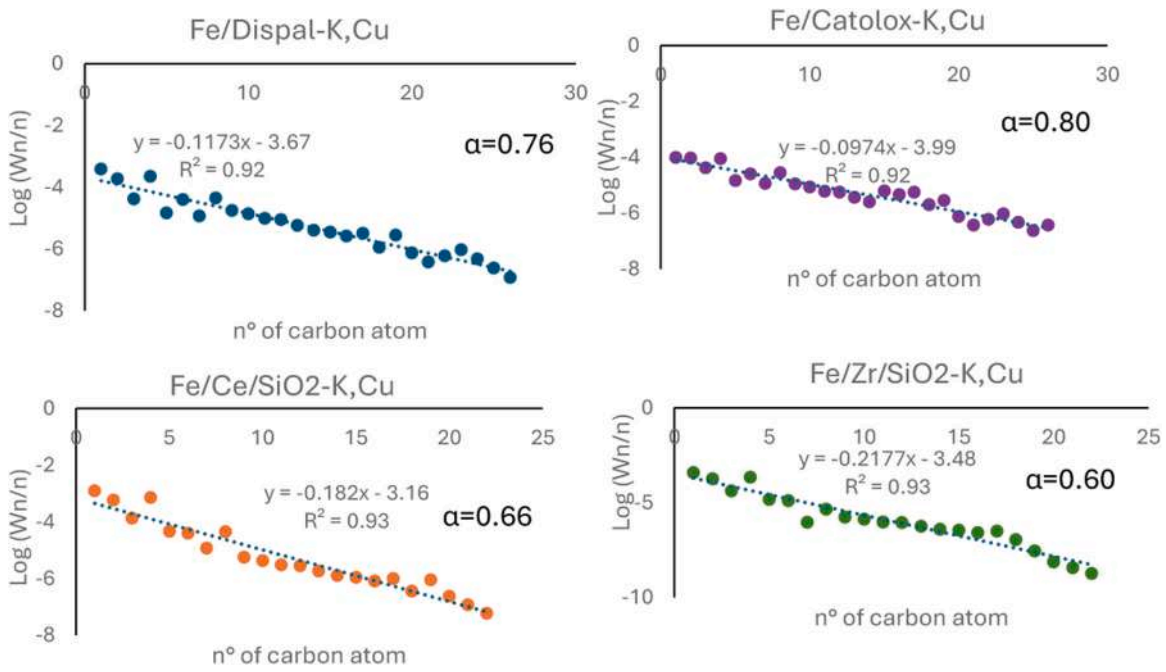

Fig. 23. Anderson-Schulz-Flory (ASF) plot of the natural logarithm of the mole fraction for all iron catalysts, Fe/Dispal-K,Cu, Fe/Catalox-K,Cu, Fe/Ce/SiO_2-K,Cu and Fe/Zr/SiO_2-K,Cu.

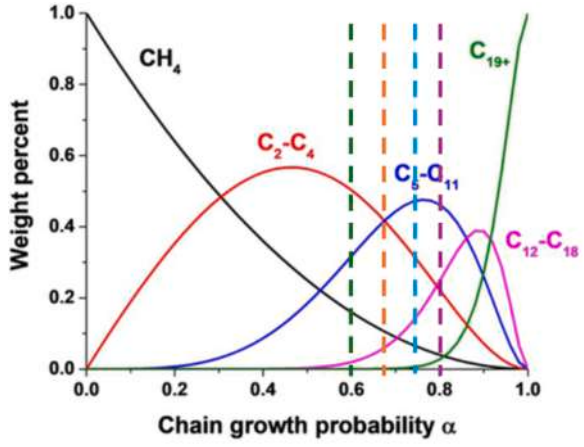

Fig. 24. Anderson-Schulz-Flory (ASF) prediction of product distribution for Fischer Tropsch synthesis, modified based on the color code of each catalyst, turquoise- Fe/Dispal-K,Cu, purple-Fe/Catalox-K,Cu, orange-Fe/Ce/SiO_2-K,Cu and green-Fe/Zr/SiO_2-K,Cu [76].

catalysts [77]. In another study, different supports were tested for iron FT catalysts, and the Al_2O_3 supported catalysts demonstrated higher CO conversion (51%) than SiO_2 supported catalysts (26%) after a CO and H_2 pretreatment at 2 MPa, H_2:CO=2 GHSV = 16 L $h^{-1}g^{-1}$ and T = 300 °C. Additionally, the C_{5+} selectivity was 64% for Fe/Al_2O_3 compared to 60% for Fe/SiO_2 [10,78,79]. As for the reason why metallosilicate supported iron catalysts outperformed plain silica supported iron catalysts, the promotional impact of the metal in the metallosilicates and mesoporous structure that remain intact during the reaction could explain it. The metal in the metallosilicates serves as a promoter that enhances the catalytic activity, while the mesoporous structure facilitates mass transfer and reactant accessibility to the active sites, resulting in higher CO conversion and C_{5+} selectivity [17,80–82].

The SEM images suggests that the metals are embedded within the alumina support, rendering it more difficult for reactants to reach the active metal sites, which accounts for the lower activity of the alumina-supported catalysts (Fig. 18) Although the BET surface of the Catalox supported catalyst was lower than that of the Dispal supported catalyst, Fe/Catalox-K,Cu had an ordered mesoporous structure while the pore structure of Fe/Dispal-K,Cu was ill-defined. This structural difference may have contributed to the higher catalytic activity of the former catalyst. The spherical (donut) morphology of the catalyst particles could improve stability of the Sasol-supported catalyst by offering high surface area to volume ratio, which means that there are more active sites on the catalyst surface. The uniformity of the spherical shape reduces diffusion limitations, pressure drop and increase attrition resistance [54,83]. Our findings suggest that all the catalysts are characterized by excellent stability during the time of reaction for all the duration of our test (about 90 h) (Supporting document, Figure 6).

4. Conclusion

Iron metallosilicates operate at higher temperatures compared to Co catalysts, which reduces the cooling coil surface area. Typically, Fe catalyst produce more light gases than Co, but the iron metallosilicates, with K and Cu promoters, were capable of producing a hydrocarbon distribution at 300 °C similiar to cobalt metallosilicates operating at 220 °C. The K and Cu on the metallosilicates increased conversion 20% compared to unsupported iron metallosilicates. For example, in our previous study at the same conditions the unsupported iron metallosilicates converted 68% of the CO for the Fe/Ce/SiO_2 and 52% for the Fe/Zr/SiO_2 catalysts. It reached 85% and 75% at the same conditions 325 °C and 20 bar for these two supports with K and Cu. A further innovation is that rather than a bulk catalyst we applied the NHSG method to synthesize iron catalyst on commercial Sasol supports Catalox and Dispal. CO conversion over the Catalox exceeded 85% at 325 °C and 20 bar while the C_{7+} selectivity was 57%. The catalyst composition was stable with time. On the other hand, the Dispal supported catalyst converted 78% of the CO with only 38% C_{7+} selectivity at the same conditions. Both type of catalysts exhibited similar stability throughout the reaction process. Metallosilicates have better activity until the temperature 300 °C. To further advance the study of the non-hydrolytic sol-gel method, optimizing the reaction kinetics through in-depth analysis is essential. Substituting the iron nitrate with iron chloride is

a future avenue of research to improve catalyst performance. Pt and Mo are other potential promoters to increase conversion and reduce light gas production. By adjusting the quantity of K and Cu promoters, it may be possible to not only decrease carbon dioxide production, but also enhance C_{7+} selectivity.

CRediT authorship contribution statement

Tugce N. Eran: Writing – review & editing, Writing – original draft, Visualization, Validation, Software, Project administration, Methodology, Investigation, Formal analysis, Data curation, Conceptualization. **Gregory Patience:** Writing – original draft, Supervision, Resources, Project administration, Funding acquisition. **Arian Grainca:** Writing – review & editing, Writing – original draft, Visualization, Formal analysis, Data curation. **Jean Guyot:** Writing – original draft, Methodology, Formal analysis, Data curation, Conceptualization. **Carlo Pirola:** Writing – review & editing, Writing – original draft, Visualization, Supervision, Resources, Project administration, Investigation, Funding acquisition, Conceptualization. **Federico Galli:** Writing – original draft, Supervision, Project administration, Conceptualization. **Josianne Lefebvre:** Writing – review & editing, Visualization, Validation, Software, Formal analysis, Data curation.

Declaration of Competing Interest

The authors declare that they have no known competing financial interests or personal relationships that could have appeared to influence the work reported in this paper.

Data Availability

Data will be made available on request.

Acknowledgment

This research was undertaken, in part, thanks to funding from the Canada Research Chairs program (950-231476) and Canada Foundation for Innovation (FCI 36788). This work has been partially funded by Piano di Sostegna alla Ricerca (PSR 2021). Action A of the Dipartimento di Chimica, Università degli Studi di Milano. The Collegues Prof. Laura Prati and Prof. Alessandro Minguzzi are warmly thanked for their support contribution to the work with the PNRR Spoke 9- PE2 project with the Politecnico di Milano.

Appendix A. Supporting information

Supplementary data associated with this article can be found in the online version at doi:10.1016/j.cattod.2024.114655.

References

[1] H. Xiong, Y. Zhang, K. Liew, J. Li, Catalytic performance of zirconium-modified Co/Al_2O_3 for Fisher-Tropsch synthesis, J. Mol. Catal. A: Chem. 231 (2005) 145–151.
[2] Ø. Borg, S. Eri, E.A. Blekkan, S. Storsæter, H. Wigum, E. Rytter, A. Holmen, Fisher-Tropsch synthesis over γ -alumina-supported cobalt catalysts: Effect of support variables, J. Catal. 248 (2007) 89–100.
[3] H.M.T. Galvis, A.C. Koeken, J.H. Bitter, T. Davidian, M. Ruitenbeek, A.I. Dugulan, K.P. de Jong, Effects of sodium and sulfur on catalytic performance of supported iron catalysts for the Fisher-Tropsch synthesis of lower olefins, J. Catal. 303 (2013) 22–30.
[4] F. Lu, X. Chen, Z. Lei, L. Wen, Y. Zhang, Revealing the activity of different iron carbides for Fisher-Tropsch synthesis, Appl. Catal. B: Environ. 281 (2021) 119521.
[5] F. Song, X. Yong, X. Wu, W. Zhang, Q. Ma, T. Zhao, M. Tan, Z. Guo, H. Zhao, G. Yang, et al., FeMn@HZSM-5 capsule catalyst for light olefins direct synthesis via Fisher-Tropsch synthesis: Studies on depressing the co2 formation, Appl. Catal. B: Environ. 300 (2022) 120713.
[6] Y. Yang, H.-W. Xiang, Y.-Y. Xu, L. Bai, Y.-W. Li, Effect of potassium promoter on precipitated iron-manganese catalyst for Fischer–Tropsch synthesis, Appl. Catal. A: Gen. 266 (2) (2004) 181–194.
[7] S. Li, S. Krishnamoorthy, A. Li, G.D. Meitzner, E. Iglesia, Promoted iron-based catalysts for the Fischer–Tropsch synthesis: design, synthesis, site densities, and catalytic properties, J. Catal. 206 (2) (2002) 202–217.
[8] C.-H. Zhang, Y. Yang, B.-T. Teng, T.-Z. Li, H.-Y. Zheng, H.-W. Xiang, Y.-W. Li, Study of an iron-manganese Fischer–Tropsch synthesis catalyst promoted with copper, J. Catal. 237 (2) (2006) 405–415.
[9] W. Ngantsoue-Hoc, Y. Zhang, R.J. O'Brien, M. Luo, B.H. Davis, Fischer-Tropsch synthesis: activity and selectivity for group I alkali promoted iron-based catalysts, Appl. Catal. A: Gen. 236 (1-2) (2002) 77–89.
[10] K. Cheng, V.V. Ordomsky, B. Legras, M. Virginie, S. Paul, Y. Wang, A.Y. Khodakov, Sodium-promoted iron catalysts prepared on different supports for high temperature Fisher-Tropsch synthesis, Appl. Catal. A: Gen. 502 (2015) 204–214.
[11] R.J. O'Brien, B.H. Davis, Impact of copper on an alkali promoted iron Fisher-Tropsch catalyst, Catal. Lett. 94 (2004) 1–6.
[12] D.B. Bukur, D. Mukesh, S.A. Patel, Promoter effects on precipitated iron catalysts for Fischer-Tropsch synthesis, Ind. Eng. Chem. Res. 29 (2) (1990) 194–204.
[13] H. Wan, B. Wu, C. Zhang, H. Xiang, Y. Li, Promotional effects of Cu and K on precipitated iron-based catalysts for Fisher-Tropsch synthesis, J. Mol. Catal. A: Chem. 283 (1-2) (2008) 33–42.
[14] Z. Ni, X. Zhang, J. Bai, Z. Wang, X. Li, Y. Zhang, Potassium promoted core–shell-structured FeK@SiO_2 catalysts used for Fischer–Tropsch synthesis to olefins without further reduction, N. J. Chem. 44 (1) (2020) 87–94.
[15] S. Li, A. Li, S. Krishnamoorthy, E. Iglesia, Effects of Zn, Cu, and K promoters on the structure and on the reduction, carburization, and catalytic behavior of iron-based Fischer–Tropsch synthesis catalysts, Catal. Lett. 77 (4) (2001) 197–205.
[16] H. Chang, Q. Lin, M. Cheng, K. Zhang, B. Feng, J. Chai, Y. Lv, Z. Men, Effects of potassium loading over iron–silica interaction, phase evolution and catalytic behavior of precipitated iron-based catalysts for Fisher-Tropsch synthesis, Catalysts 12 (8) (2022) 916.
[17] T.N. Eran, F. Galli, F. Mazzoni, M. Longhi, A. Grainca, G. Patience, C. Pirola, Metallosilicates as an iron support to catalyze Fisher-Tropsch synthesis, Catal. Today 404 (2022) 132–141.
[18] E. Tranquillo, F. Bollino, Surface modifications for implants lifetime extension: an overview of sol-gel coatings, Coatings 10 (6) (2020) 589.
[19] D. Navas, S. Fuentes, A. Castro-Alvarez, E. Chavez-Angel, Review on sol-gel synthesis of perovskite and oxide nanomaterials, Gels 7 (4) (2021) 275.
[20] A. Corma, From microporous to mesoporous molecular sieve materials and their use in catalysis, Chem. Rev. 97 (6) (1997) 2373–2420.
[21] A. Taguchi, F. Schüth, Ordered mesoporous materials in catalysis, Microporous Mesoporous Mater. 77 (1) (2005) 1–45.
[22] S.S. Prakash, C.J. Brinker, A.J. Hurd, S.M. Rao, Silica aerogel films prepared at ambient pressure by using surface derivatization to induce reversible drying shrinkage, Nature 374 (6521) (1995) 439–443.
[23] G. Pajonk, Aerogel catalysts, Appl. Catal. 72 (2) (1991) 217–266.
[24] D.P. Debecker, P.H. Mutin, Non-hydrolytic sol–gel routes to heterogeneous catalysts, Chem. Soc. Rev. 41 (9) (2012) 3624–3650.
[25] V. Smeets, A. Styskalik, D.P. Debecker, Non-hydrolytic sol–gel as a versatile route for the preparation of hybrid heterogeneous catalysts, J. Sol. -Gel Sci. Technol. 97 (2021) 505–522.
[26] J. Wentrup, G.R. Pesch, J. Thöming, Dynamic operation of Fisher-Tropsch reactors for power-to-liquid concepts: A review, Renew. Sustain. Energy Rev. 162 (2022) 112454.
[27] J. Aluha, Y. Hu, N. Abatzoglou, Effect of co concentration on the α -value of plasma-synthesized co/c catalyst in fischer-tropsch synthesis, Catalysts 7 (2) (2017) 69.
[28] G.S. Pokrovski, J. Schott, F. Farges, J.-L. Hazemann, Iron (iii)-silica interactions in aqueous solution: Insights from x-ray absorption fine structure spectroscopy, Geochim. Et. Cosmochim. Acta 67 (19) (2003) 3559–3573.
[29] A.S. Kinsela, A.M. Jones, M.W. Bligh, A.N. Pham, R.N. Collins, J.J. Harrison, K. L. Wilsher, T.E. Payne, T.D. Waite, Influence of dissolved silicate on rates of Fe(ii) oxidation, Environ. Sci. Technol. 50 (21) (2016) 11663–11671.
[30] N. Lohitharn, J.G. Goodwin Jr, E. Lotero, Fe-based Fisher-Tropsch synthesis catalysts containing carbide-forming transition metal promoters, J. Catal. 255 (1) (2008) 104–113.
[31] D.A. Ward, E.I. Ko, Preparing catalytic materials by the sol-gel method, Ind. Eng. Chem. Res. 34 (2) (1995) 421–433.
[32] C. Milea, C. Bogatu, A. Duta, The influence of parameters in silica sol-gel process, Bull. Transilv. Univ. Brasov 4 (2011) 53.
[33] S. Vives, C. Meunier, Influence of the synthesis route on sol–gel SiO_2 –TiO_2 (1: 1) xerogels and powders, Ceram. Int. 34 (1) (2008) 37–44.
[34] G. Kamath, S. Badoga, A.K. Dalai, Synthesis and application of metallosilicate supports for cobalt-based Fisher-Tropsch synthesis catalyst, Energy Fuels 33 (1) (2018) 551–560.
[35] K.V. Kumar, S. Gadipelli, B. Wood, K.A. Ramisetty, A.A. Stewart, C.A. Howard, D. J. Brett, F. Rodriguez-Reinoso, Characterization of the adsorption site energies and heterogeneous surfaces of porous materials, J. Mater. Chem. A 7 (17) (2019) 10104–10137.
[36] R. Bardestani, G.S. Patience, S. Kaliaguine, Experimental methods in chemical engineering: specific surface area and pore size distribution measurements–BET, BJH, and DFT, Can. J. Chem. Eng. 97 (11) (2019) 2781–2791.
[37] F.J. Sotomayor, K.A. Cychosz, M. Thommes, et al., Characterization of micro/mesoporous materials by physisorption: concepts and case studies, Acc. Mater. Surf. Res. 3 (2) (2018) 34–50.
[38] K.S. Sing, R.T. Williams, Physisorption hysteresis loops and the characterization of nanoporous materials, Adsorpt. Sci. Technol. 22 (10) (2004) 773–782.

[39] S. Fu, Q. Fang, A. Li, Z. Li, J. Han, X. Dang, W. Han, Accurate characterization of full pore size distribution of tight sandstones by low-temperature nitrogen gas adsorption and high-pressure mercury intrusion combination method, Energy Sci. Eng. 9 (1) (2021) 80–100.

[40] K. Karásková, K. Pacultová, T. Bílková, D. Fridrichová, M. Koštejn, P. Peikertová, P. Stelmachowski, P. Kukula, L. Obalová, Effect of zinc on the structure and activity of the cobalt oxide catalysts for NO decomposition, Catalysts 13 (2023) 18.

[41] E. Bertolucci, A.M.R. Galletti, C. Antonetti, M. Marracci, B. Tellini, F. Piccinelli, C. Visone, Chemical and magnetic properties characterization of magnetic nanoparticles, In: 2015 IEEE International Instrumentation and Measurement Technology Conference (I2MTC) Proceedings, IEEE, 2015, 1492-1496.

[42] K.-S. Loh, Y.H. Lee, A. Musa, A.A. Salmah, I. Zamri, Use of Fe_3O_4 nanoparticles for enhancement of biosensor response to the herbicide 2, 4-dichlorophenoxyacetic acid, Sensors 8 (9) (2008) 5775–5791.

[43] M. Zainuri, Hematite from natural iron stones as microwave absorbing material on x-band frequency ranges, vol. 196. IOP conference series: materials science and engineering, IOP Publishing, 2017.

[44] V. Kumar, S. Chahal, D. Singh, A. Kumar, P. Kumar, K. Asokan, Annealing effect on the structural and dielectric properties of hematite nanoparticles, vol. 1953. AIP Conference Proceedings, AIP Publishing LLC, 2018, p. 30245. vol. 1953.

[45] G.B. Singh, C. Sonat, E. Yang, C. Unluer, Performance of MgO and MgO–SiO_2 systems containing seeds under different curing conditions, Cem. Concr. Compos. 108 (2020) 103543.

[46] G. Jayakumar, A.A. Irudayaraj, A.D. Raj, Particle size effect on the properties of cerium oxide (CeO_2) nanoparticles synthesized by hydrothermal method, Mechanics, Mater. Sci. Eng. J. 9 (1) (2017).

[47] C. Ashok, K.V. Rao, C.S. Chakra, Structural analysis of CuO nanomaterials prepared by novel microwave assisted method, J. At. Mol. 4 (5) (2014) 803–806.

[48] S.A. ArSayed, N.I. Beedri, V.S. Kadam, H.M. Pathan, Rose bengal-sensitized nanocrystalline ceria photoanode for dye-sensitized solar cell application, Bull. Mater. Sci. 39 (2016) 1381–1387.

[49] I. Joni, L. Nulhakim, M. Vanitha, C. Panatarani, Characteristics of crystalline silica (SiO_2) particles prepared by simple solution method using sodium silicate (Na_2SiO_3) precursor, vol. 1080. Journal of Physics: Conference Series, IOP Publishing, 2018, p. 12006. vol. 1080.

[50] S. Ding, J. Zhao, Q. Yu, Effect of zirconia polymorph on vapor-phase ketonization of propionic acid, Catalysts 9 (2019) 768.

[51] O. Mangla, S. Roy, Monoclinic zirconium oxide nanostructures having tunable band gap synthesized under extremely non-equilibrium plasma conditions, Multidiscip. Digit. Publ. Inst. Proc. 3 (2018) 10.

[52] E.I. Mabaso, E.v. Steen, M. Claeys, Fischer-tropsch synthesis on supported iron crystallites of different size (2006).

[53] Y. Liu, J.-F. Chen, Y. Zhang, The effect of pore size or iron particle size on the formation of light olefins in Fisher-Tropsch synthesis, RSC Adv. 5 (37) (2015) 29002–29007.

[54] J.-X. Liu, P. Wang, W. Xu, E.J. Hensen, Particle size and crystal phase effects in Fisher-Tropsch catalysts, Engineering 3 (4) (2017) 467–476.

[55] L. Zhuang, W. Zhang, Y. Zhao, H. Shen, H. Lin, J. Liang, Preparation and characterization of Fe_3O_4 particles with novel nanosheets morphology and magnetochromatic property by a modified solvothermal method, Sci. Rep. 5 (1) (2015) 9320.

[56] H. Husin, T. Asnawi, A. Firdaus, H. Husaini, I. Ibrahim, F. Hasfita, Solid catalyst nanoparticles derived from oil-palm empty fruit bunches (OP-EFB) as a renewable catalyst for biodiesel production, vol. 358. IOP Conference Series: Materials Science and Engineering, IOP Publishing, 2018, p. 12008. vol. 358.

[57] S. Suresh, S. Karthikeyan, K. Jayamoorthy, FTIR and multivariate analysis to study the effect of bulk and nano copper oxide on peanut plant leaves, J. Sci.: Adv. Mater. Devices 1 (3) (2016) 343–350.

[58] J. Sarkar, N. Chakraborty, A. Chatterjee, A. Bhattacharjee, D. Dasgupta, K. Acharya, Green synthesized copper oxide nanoparticles ameliorate defence and antioxidant enzymes in Lens culinaris, Nanomaterials 10 (2) (2020) 312.

[59] S.A. Ansari, Q. Husain, Immobilization of kluyveromyces lactis β galactosidase on concanavalin a layered aluminium oxide nanoparticles—its future aspects in biosensor applications, J. Mol. Catal. B: Enzym. 70 (3-4) (2011) 119–126.

[60] J. Thanuja, G. Nagaraju, H.R. Naika, Biosynthesis of Cu_4O_3 nanoparticles using razma seeds: Application to antibacterial and cytotoxicity activities, SN Appl. Sci. 1 (2019) 1–12.

[61] J. Moulder, J. Chastain, Handbook of X-ray Photoelectron Spectroscopy: A Reference Book of Standard Spectra for Identification and Interpretation of XPS Data, Physical Electronics Division, Perkin-Elmer Corporation, 1992.

[62] M. Mohai, Xps multiquant: multimodel XPS quantification software, Surf. Interface Anal.: Int. J. devoted Dev. Appl. Tech. Anal. Surf., Interfaces thin films 36 (8) (2004) 828–832.

[63] J. Blanchard, N. Abatzoglou, Nano-iron carbide synthesized by plasma as catalyst for Fisher-Tropsch synthesis in slurry reactors: The role of iron loading and k, cu promoters, Catal. Today 237 (2014) 150–156.

[64] H. Xiong, M. Moyo, M.A. Motchelaho, L.L. Jewell, N.J. Coville, Fisher-Tropsch synthesis over model iron catalysts supported on carbon spheres: The effect of iron precursor, support pretreatment, catalyst preparation method and promoters, Appl. Catal. A: Gen. 388 (1-2) (2010) 168–178.

[65] V.R.R. Pendyala, G. Jacobs, M.K. Gnanamani, Y. Hu, A. MacLennan, B.H. Davis, Selectivity control of Cu promoted iron-based Fisher-Tropsch catalyst by tuning the oxidation state of Cu to mimic K, Appl. Catal. A: Gen. 495 (2015) 45–53.

[66] M. Martinelli, C.G. Visconti, L. Lietti, P. Forzatti, C. Bassano, P. Deiana, CO_2 reactivity on Fe–Zn–Cu–K Fisher-Tropsch synthesis catalysts with different k-loadings, Catal. Today 228 (2014) 77–88.

[67] Ş. Özkara-Aydınoğlu, Ö. Ataç, Ö.F. Gül, Ş. Kınayyiğit, S. Şal, M. Baranak, İ. Boz, α -olefin selectivity of Fe–Cu–K catalysts in Fisher-Tropsch synthesis: Effects of catalyst composition and process conditions, Chem. Eng. J. 181 (2012) 581–589.

[68] W.D. Shafer, M.K. Gnanamani, U.M. Graham, J. Yang, C.M. Masuku, G. Jacobs, B. H. Davis, Fisher-Tropsch: product selectivity–the fingerprint of synthetic fuels, Catalysts 9 (3) (2019) 259.

[69] G. Yu, B. Sun, Y. Pei, S. Xie, S. Yan, M. Qiao, K. Fan, X. Zhang, B. Zong, Fe_x O_y C spheres as an excellent catalyst for Fischer-Tropsch synthesis, J. Am. Chem. Soc. 132 (3) (2010) 935–937.

[70] A.S. Ismail, M. Casavola, B. Liu, A. Gloter, T.W. van Deelen, M. Versluijs, J. D. Meeldijk, O. Stephan, K.P. de Jong, F.M. de Groot, Atomic-scale investigation of the structural and electronic properties of cobalt–iron bimetallic Fisher-Tropsch catalysts, ACS Catal. 9 (2019) 7998–8011.

[71] B. Xu, Y. Fan, Y. Zhang, N. Tsubaki, Pore diffusion simulation model of bimodal catalyst for Fisher-Tropsch synthesis, AIChE J. 51 (7) (2005) 2068–2076.

[72] L. Fan, K. Yokota, K. Fujimoto, Supercritical phase Fischer-Tropsch synthesis: Catalyst pore-size effect, AIChE J. 38 (10) (1992) 1639–1648.

[73] N. Tsubaki, Y. Zhang, S. Sun, H. Mori, Y. Yoneyama, X. Li, K. Fujimoto, A new method of bimodal support preparation and its application in Fisher-Tropsch synthesis, Catal. Commun. 2 (10) (2001) 311–315.

[74] J.-Y. Cheon, S.-H. Kang, J.W. Bae, S.-J. Park, K.-W. Jun, G. MuraliDhar, K.-Y. Lee, Effect of active component contents to catalytic performance on fe-cu-k/zsm5 Fisher-Tropsch catalyst, Catal. Lett. 134 (2010) 233–241.

[75] K. Okabe, M. Wei, H. Arakawa, Fischer- tropsch synthesis over cobalt catalysts supported on mesoporous metallo-silicates, Energy Fuels 17 (4) (2003) 822–828.

[76] Z. Tian, C. Wang, Z. Si, Y. Wang, L. Chen, Q. Liu, Q. Zhang, Y. Xu, L. Ma, Product distributions of fischer-tropsch synthesis over core-shell catalysts: The effects of diverse shell thickness, ChemistrySelect 3 (44) (2018) 12415–12423.

[77] S. Mosallanejad, B.Z. Dlugogorski, E.M. Kennedy, M. Stockenhuber, On the chemistry of iron oxide supported on γ -alumina and silica catalysts, ACS Omega 3 (5) (2018) 5362–5374.

[78] S.C. Kang, K.-W. Jun, Y.-J. Lee, Effects of the CO/CO_2 ratio in synthesis gas on the catalytic behavior in Fischer–Tropsch synthesis using K/Fe –Cu–Al catalysts, Energy fuels 27 (11) (2013) 6377–6387.

[79] A.Y. Khodakov, W. Chu, P. Fongarland, Advances in the development of novel cobalt Fischer-Tropsch catalysts for synthesis of long-chain hydrocarbons and clean fuels, Chem. Rev. 107 (5) (2007) 1692–1744.

[80] D.V. Peron, A.J. Barrios, A. Taschin, I. Dugulan, C. Marini, G. Gorni, S. Moldovan, S. Koneti, R. Wojcieszak, J.W. Thybaut, et al., Active phases for high temperature Fisher-Tropsch synthesis in the silica supported iron catalysts promoted with antimony and tin, Appl. Catal. B: Environ. 292 (2021) 120141.

[81] F. Farias, R. RabeloNeto, M. Baldanza, M. Schmal, F. Fernandes, Effect of K promoter on the structure and catalytic behavior of supported iron-based catalysts in Fisher-Tropsch synthesis, Braz. J. Chem. Eng. 28 (2011) 495–504.

[82] A. Wielers, A. Kock, C. Hop, J. Geus, A. van Der Kraan, The reduction behavior of silica-supported and alumina-supported iron catalysts: A Mössbauer and infrared spectroscopic study, J. Catal. 117 (1) (1989) 1–18.

[83] M. Mandic, B. Todic, L. Zivanic, N. Nikacevic, D.B. Bukur, Effects of catalyst activity, particle size and shape, and process conditions on catalyst effectiveness and methane selectivity for Fisher-Tropsch reaction: a modeling study, Ind. Eng. Chem. Res. 56 (10) (2017) 2733–2745.